Diverse Permian magmatism in the Tarim Block, NW China: genetically linked to the Permian Tarim mantle plume?

Chuan-Lin Zhang[a]*, Yi-Gang Xu[b], Zheng-Xiang Li[c], Hong-Yan Wang[a], Hai-Min Ye[a]

[a] *Nanjing Institute of Geology and Mineral Resources, CGS, Nanjing 210016, P. R. China*

[b] *Key Laboratory of Isotope Geochronology and Geochemistry, Guangzhou Institute of Geochemistry, Chinese Academy of Sciences, Guangzhou, 510640, China*

[c] *The Institute for Geoscience Research (TIGeR), Department of Applied Geology, Curtin University of Technology, GPO Box U1987, Perth WA 6845, Australia*

*Corresponding author

E-mail: zchuanlin@yahoo.com.cn

Tel: 86-25-84897912

Fax: 86-25-84600446

Abstract

Zircon U-Pb ages and geochemical data are reported for the Piqiang oxide-bearing ultramfic-mafic complex, the Bachu mafic dyke swarm, the Yingan and Kaipaizileike basalts and the Halajun A-type granites in the Tarim Block, Northwest China. The Piqiang complex and the Halajun A-type granites were emplaced at ca. 276 Ma and ca. 278 Ma, respectively. Together with previously reported geochronological data, the diverse intrusive and extrusive rocks in Tarim show a peak age at ca. 275 Ma. Elemental and Nd isotope geochemistry suggests that the spatially and temporally related Piqiang complex (including some dolerite dykes or stocks) and the Halajun A-type granites were formed via crystal fractionation/accumulation of a common plume-derived parental mafic magma (melting degree > 10%), coupled with variable extents of crustal contamination. Crystal fractionation/accumulation in one or several magma chambers resulted in the diversity of rocks types. The Bachu mafic dyke swarm shares a similar mantle source with the intrusive rocks in the Piqiang-Halajun area but with a relatively lower degree of partial melting (~5%). In contrast, the basalts were derived from a time-integrated, enriched lithospheric mantle source as suggested by their high-Ti, LREE- and LILE-enriched trace element signature and negative $\varepsilon_{Nd}(T)$ values (-2.0 ~ -2.6). The synchronous yet diverse range of Permian igneous rocks in Tarim can best be accounted for by a Permian mantle plume, which is about 15 Ma earlier than the Emeishan plume in southwestern China.

Key words: ultramafic-mafic complex; mafic dyke swarm; A-type granites; basalts; Permian Tarim LIP; mantle plume; NW China

1. Introduction

Mantle plumes are thermal anomalies that rise from the lower mantle or even the core–mantle boundary (Campbell and Griffiths, 1990). The ascent of a mantle plume can cause melting in the mantle and the crust, resulting in the formation of diverse igneous rocks (Bryan and Ernst, 2008; Xu et al., 2008). The diversity of extrusive and intrusive rocks genetically related to a single mantle plume is well documented in the Siberian traps (Czamanske et al., 1995; Fedorenko and Czamanske, 1997; Arndt et al., 1998, 2003), the Emeishan large igneous province (ELIP) (Xu et al., 2004, 2007, 2008; Zhou et al., 2002, 2008; Wang et al., 2008) and even in some Precambrian large igneous provinces (Ernst et al., 2008; Li X.H. et al., 2003; Li Z.X. et al., 2008). Such diversity has been attributed to the variability in mantle sources, variable degrees of plume-lithosphere interaction, variable degrees of crustal melting and assimilation, or a combination of these processes (Arndt et al., 1998, 2003; Zhou et al., 2008, 2009; Wang et al., 2009).

Recent work suggests that a possible mantle plume was responsible for the early to middle Permian large igneous province in Tarim and the southern part of the Central Asian Orogenic Belt (CAOB) (Zhou et al., 2004; Chen et al., 2006; Borisenko et al., 2006; Mao et al., 2008; Pirajno et al., 2008, 2009; Polyakov et al., 2008; Zhang et al., 2008, 2010; Zhou et al., 2009; Tian et al., 2010) (Fig. 1), which was termed the Tarim LIP by Borisenko et al. (2006; also known as Bachu LIP or Tarim-Bachu LIP, *e.g.*, Zhang et al., 2008, 2010; Pirajno et al., 2009). However, the genetic links between the intrusive and extrusive rocks in the Tarim LIP, especially those in the Tarim Block, have not yet been established and thus the processes that formed the diverse igneous rocks are not well understood. In this study, we carried out geological, geochronological and geochemical analyses on the Piqiang oxide-bearing intrusive complex, the Halajun granite plutons (pluton □ and pluton □), the Bachu mafic dyke swarm and basalts in the Tarim Block, NW China. The aims of the study were to constrain the timing of the emplacements and to address the petrogenesis of these diverse igneous rocks by identifying possible sources involved in magma generation and deciphering their relationship to the mantle plume.

2. Regional geology and petrography

The Tarim Block in northwestern China covers an area of more than 600,000 km^2. It is one of the least known continental blocks in Asia due to its extensive coverage by desert. Nevertheless, several important phases of igneous activities have been identified in Tarim, *i.e.*, the Neoarchaean, early Palaeoproterozoic, Neoproterozoic and early Permian events (Hu et al., 2000; Lu et al., 2008; Zhang et al., 2007, 2008, 2010). Among these igneous activities, the early Permian phase is the latest and was considered to be related to mantle plume activity (Pirajno et al., 2008; Mao et al., 2008; Zhou et al., 2009; Zhang et al., 2008, 2010; Tian et al., 2010).

The study region is close to Bachu in the northwestern part of the Tarim Block (Figs. 1 and 2). Some geological, geochronological and geochemical data have previously been reported on the ultramafic-mafic-syenite complex, mafic dykes and syenite plutons (or dykes) in the Bachu region, and on the basalts in the Yingan and Kaipaizileike sections (marked as KF1 and KF2 in Fig. 1) (Rui et al., 2002; Jiang et al., 2004a, 2004b; Yang et al., 1995, 2005, 2006, 2007; Li et al., 2007; Zhou et al., 2009). However, most of these data are published in the Chinese literature and precise geochronology and systematic geochemical data are still scarce, and no age and geochemical data have yet been reported for the oxide (magnetite)-bearing Piqiang ultramafic-mafic complex and the nearby Halajun granites.

2.1 The Piqiang ultramafic-mafic complex

The oxide (magnetite)-bearing Piqiang intrusive complex crops out ca. 120 km northeast of Atushi City (Fig. 2a). It intrudes Devonian sedimentary rocks with the contact dipping 70 - 80° toward the interior of the complex, and has an outcrop area of ca. 25 km^2 (Fig. 2a). Thin-section examinations and field observations, together with previous field mapping and petrographic studies (*e.g.*, Rui et al., 2002), indicate that the complex is composed mainly of gabbro (accounting for ca. 95% of the outcrop) with minor olivine-bearing gabbro and dolerite (Fig. 2b). Most of the crystalline rocks are cumulates (except for the dolerite). The gabbros are medium- to coarse-grained, and consist of clinopyroxene (30–50%), plagioclase (40–45%) and variable amounts of orthopyroxene (5-15%), magnetite (5-20%, mostly vanadium titano - magnetite) and olivine (1-10%). Accessory minerals include apatite and zircon. Magnetite is commonly disseminated in the gabbros but in places it occurs as veins or blocks, forming economic orebodies (Fig. 2b). The dolerite is fine-grained or microcrystalline and consists mainly of plagioclase (45-55%), clinopyroxene (35-45%) and Ti-Fe oxides (5-10%). No phenocrysts have been observed.

One sample (08KT01) collected from coarse-grained gabbro in the Piqiang complex (08KT01, 40º24′42″N, 77º38′10″E) was selected for U-Pb zircon dating. Eleven gabbro cumulates and two dolerite samples were chosen for geochemical analyses.

2.2 The Bachu mafic dyke swarm

Mafic dykes around the Wajilitage complex intrude the upper Devonian sedimentary rocks with variable strikes (Fig.1, Fig. 2c). The local geological map (1:5000) shows that the dykes also intrude the Wajilitage layered ultramafic-mafic-syenite complex (Fig. 2c) and some of them intermingle with the complex. At several outcrops bimodal dykes, consisting of dolerite and syenite, have been observed. The petrography of the mafic dykes around Wajillitage is similar to that in the Mazaertage area (also known as the Xiaohaizi area) north of the Wajilitage complex (Jiang et al., 2004a; Yang et al., 2007; Zhou et al., 2009). According to Jiang et al. (2004a) and our own field observations, the mafic dyke swarm in the Mazaertage area mainly crops out around the Xiaohaizi gabbro-syenite complex with variable strike directions (Fig. 1), as with the mafic dyke swarm in the Wajilitage area (this study). The widths of the dykes from both areas range mostly between ~2 m and ~30 cm, with a few exceptions of over 5 m wide. Sixteen samples were collected from the Wajilitage dolerite dykes for geochemical analyses (Fig. 2c).

2.3 The Halajun granite plutons

Two granite plutons crop out at Halajun (termed Halajun pluton I and II), near the Piqiang complex (Fig. 2a). Pluton I, with a ca. 40 km^2 outcrop area, intrudes the upper Carboniferous sedimentary rocks with the contact dipping 50-60° outward (Fig. 2a). A hornfels belt, 10 – 30 m wide, developed along the margin of the pluton. The granites are pinkish in color and medium- to coarse-grained. The main minerals are alkali feldspar (60–65%), quartz (35-40%), hornblende (~2 %) and brown biotite (~1%). Accessory minerals include zircon, apatite and Fe-Ti oxides. Pluton □ has an outcrop area of ca. 50 km^2 surrounded by the desert. This pluton is characterized by a coarse-grained texture (up to 1 cm) and a rather uniform mineralogical composition. The rock-forming minerals are quartz (~40%), alkali feldspar (~60%) and very minor hornblende. The coarse-grained texture of this pluton and the coverage of its margins by the desert indicate that the pluton is likely much larger than its outcrop area.

One sample each from Halajun pluton □ (08KT02: 46º35′8″N, 90º11′57″E) and pluton □ (08KT03: 46º15′34″N, 90º48′45″E) were selected for zircon U-Pb geochronology. Additional samples were collected from the two plutons for geochemical analyses.

2.4 Permian basalts in Yingan and Kaipaizileike

The Permian basaltic sections in Yingan and Kaipaizileike have been described by Jiang et al. (2004b) and Zhou et al. (2009). The rock successions have been subdivided into the Kupukuziman Formation (KF1) and the overlying Kaipaizikelei Formation (KF2) (Fig. 1). KF1 is dominated by basaltic flows interlayered with valcaniclastic rocks, and KF2 is mainly composed of basalts with minor fine-grained volcanic pyroclastics. Twelve basalt samples (08KT01 – 08KT12) from KF1 and three basalt samples (08KT13 – 08KT15) from KF2 were collected during this study. All the samples are of greenish color and cryptocrystalline or microcrystalline. They consist of needle-like plagioclase (40-50%), clinopyroxene (30-40%, mostly replaced by actinolite) and Ti-Fe oxides (10-20%).

3. Analytical methods

Zircon separation was carried out first using conventional magnetic and density techniques to concentrate non-magnetic, heavy fractions. Zircon grains were then hand-picked under a binocular microscope. Zircon ages were analyzed using the SHRIMP U-Pb method. Zircon grains were cast on an epoxy mount, and polished to expose the crystals in half for analyses. The inner structures of the zircon grains were documented with transmitted and reflected light photomicrographs and cathodoluminescence (CL) images. The mount was then vacuum-coated with high-purity gold. U-Th-Pb analyses were conducted at the Beijing SHRIMP Center, Chinese Academy of Geological Sciences using standard operating conditions (Williams, 1998). U-Th-Pb ratios were determined relative to the TEMORA standard zircon, and the absolute abundances of U and Th were determined using the SL13 standard zircon. Measured compositions were corrected for common Pb using non-radiogenic ^{204}Pb, and an average crustal composition (Stacey and Kramers, 1975) appropriate to the age of the mineral. Software SQUID 1.0 and ISOPLOT (Ludwig, 1999, 2001) were used for data processing. The weighted mean ages are quoted at 95% confidence level. U-Pb zircon data are presented in Data Repository Table DR1.

Geochemical and isotope measurements were carried out at the Guangzhou Institute of Geochemistry, Chinese Academy of Sciences (GIG CAS). Major elements were analyzed using a Rigaku ZSX100e XRF following the analytical procedure described by Li et al. (2004). Analytical precision is generally better than 2%. Trace elements were analyzed using a Perkin-Elmer Sciex ELAN 6000 ICP-MS following the procedure described by Li et al. (2002). In-run analytical precisions for most elements were better than 3-5%. Major and trace elements data are presented in Data Repository Table DR2.

Nd isotopes were determined using a Micromass Isoprobe multi-collector ICPMS (MC-ICPMS) at GIG CAS, following the procedure described by Li et al. (2004). Measured $^{143}Nd/^{144}Nd$ ratios were normalized to $^{146}Nd/^{144}Nd = 0.7219$. The reported $^{143}Nd/^{144}Nd$ ratios were adjusted to the Shin Etsu JNdi-1 standard $^{143}Nd/^{144}Nd = 0.512115$. Sm-Nd isotopic compositions and calculated parameters are listed in Table 1.

4 Results

4.1 U-Pb zircon ages

4.1.1 The Piqiang ultramafic-mafic complex

Zircon grains from sample 08KT01 are mostly euhedral, transparent and colorless. They are 200-300 μm long, with length to width ratios of 3–5. Euhedral concentric zoning is common in most crystals under CL images, typical of a magmatic origin. No relict cores have been observed. Eighteen analyses were conducted on 18 zircon grains. Uranium concentrations range from 61 to 531 ppm, Th from 39 to 524 ppm, and Th/U ratios from 0.42 to 1.19 (Data Repository Table DR1). Among the eighteen analyses, three analyses (spots 2.1, 7.1 and 13.1) have higher common lead and their $^{206}Pb/^{238}U$ ages deviate significantly from the other analyses. These three spots were excluded from the age calculation. The remaining 15 analyses yielded a weighted mean $^{206}Pb/^{238}U$ age of 276 ± 4 Ma (MSWD = 2.8) (Fig. 3a).

4.1.2 The Halajun granites (plutons □ and □)

Euhedral zircons from sample 08KT02 are up to 100-200 μm in length, and have length to width ratios up to 4:1. Most zircons are transparent and colourless and a few are brown and turbid. In CL images no inherited cores have been observed. Euhedral concentric zoning is common in most crystals. Fourteen analyses were obtained on 14 grains (Data Repository Table DR1). U and Th concentrations are 80–169 ppm and 34–95 ppm, respectively. Th/U ratios vary from 0.39 to 0.70. Among the fourteen analyses, spot 1.1 has a large error and was rejected from the age calculation. The remaining thirteen analyses have consistent $^{206}Pb/^{238}U$ ages within error and yielded a weighted mean $^{206}Pb/^{238}U$ age of 278 ± 3 Ma (MSWD = 0.2) (Fig. 3b). This age is interpreted as the emplacement age of the Halajun pluton I.

Zircons from sample 08KT03 are euhedral, up to 400 μm long, and have length to width ratios up to 4:1. They are transparent and colourless, without inherited cores. Euhedral concentric zoning is common, suggesting a magmatic origin. Seventeen analyses were obtained on 17 grains (Data Repository Table DR1). U concentrations range from 80 to 840 ppm, Th from 30 to 233 ppm and Th/U ratios vary within the range of 0.27–0.70. Spot 1.1 has a $^{206}Pb/^{238}U$ age of 570 ± 11 Ma and it is likely a xenocryst (a much larger grain compared with other zircons). The other 16 analyses agree within errors and yielded a weighted mean $^{206}Pb/^{238}U$ age of 278 ± 3 Ma (MSWD = 1.36) (Fig. 3c). This age is interpreted as the crystallization age of the Halajun pluton □.

4.2 Elemental geochemistry

4.2.1 Hydrothermal alteration effects

Most samples from the Piqiang complex, the Halajun granites (plutons □ and □) and the basalts have relatively low LOI (loss on ignition), thus their elemental compositions likely remained immobile since their emplacement. On the other hand, the Bachu mafic dykes have relatively high LOI (>2%; Data Repository Table DR2), suggesting that they may have been altered to various degrees during post-emplacement processes. Generally, alteration processes do not significantly affect high field strength elements (HFSE: Th, Nb, Zr, Hf, Ti, Y) and rare earth elements (REE) (Pearce, 1992), as is evidenced by the positive correlations of Zr versus La and Nb for the studied samples (Fig. 4). Thus, the variations of HFSE and REE can be used to characterize the magmatic processes (see the following section). On the contrary, LILEs (large ion lithophile elements), such as K, Na and Rb, do not show a correlation with the immobile elements, suggesting that they have been variably affected by alteration processes (Fig. 4).

4.2.2 The Piqiang ultramafic-mafic complex

Samples from the Piqiang complex show large elemental compositional variations (39.1-52.2 wt.% SiO_2, 7.8-24.3 wt.% Al_2O_3, 2.7-14.0 wt.% MgO, 6.9-11.8 wt.% CaO, 0.6-5.6 wt.% TiO_2, 5.5-25.0 wt.% $Fe_2O_3^{(t)}$, 1.01-3.52 wt.% Na_2O, 0.11-1.83 wt.% K_2O, 0.01-0.37 wt.% P_2O_5; Data Repository Table DR2, and Fig. 4), which may be related to crystal fractionation/accumulation. They straddle the line separating the alkaline and sub-alkaline fields on both the total alkali versus silica diagram and the incompatible elements classification diagram (Fig. 5). In Harker diagrams (Fig. 4), as SiO_2 decreases, MgO and Fe_2O_3 increase while Na_2O and K_2O decrease. Al_2O_3, TiO_2, and CaO show more scatter (Fig. 4). In the AFM (Na_2O+K_2O-FeO-MgO) diagram, the rocks follow a tholeiitic trend (Fig. 5).

The cumulate rocks (magnetite-bearing gabbro and olivine-bearing gabbro) from the Piqiang complex have low and variable compatible element contents, e.g., Cr concentrations ranging from 0.5 to 260 ppm, Ni from 0.1 to 173 ppm and V from 176 to 841 ppm (Data Repository Table DR2). Large variations in REE contents (∑REE = 16-149 ppm) could be ascribed to different abundances of cumulus and accessory minerals such as apatite and zircon because of their high partition coefficients for REEs. Nonetheless, all the cumulate samples are uniformly enriched in LREE relative to HREE with $(La/Yb)_N$ ranging from 2 to 8. All but one sample (KL01-6) show variable positive Eu anomalies (δEu =1.1-3.4) (Fig. 6, where both the chondrite and primitive mantle values are from Sun and McDonough, 1989). Incompatible elements also exhibit variable abundances in the primitive mantle-normalized spider-diagrams, reflecting different abundances of cumulus and accessory minerals (Fig. 6). The rocks show positive anomalies in Ba, Sr and Ti relative to neighbouring elements and depletion in P relative to Nd and Sm.

Two dolerite samples (KL01-14, KL01-15) have relatively high total REE (∑REE = 155-187 ppm) and insignificant Eu anomalies (δEu ≈ 0.95). However, they exhibit REE patterns and trace element spider-diagrams similar to the cumulate samples, except that they have higher concentrations than the cumulate samples (Fig. 6). Taking into account their coexistence on outcrops, this suggests a common origin for the dolerites and the cumulate gabbros.

4.2.3 The Bachu mafic dykes

The Bachu mafic dykes have low SiO_2 (41.9 - 45.1%, mostly <45%), MgO (2.7-6.1%), Cr (<60 ppm), Ni (<100 ppm) contents, variable total alkali (3.4-9.9%), MnO (0.05-0.20%), Al_2O_3 (12.4-16.0%), CaO (6.5-9.8%), $Fe_2O_3^T$ (7.6-17.2%) and relatively high TiO_2 (2.2-5.2%), P_2O_5 (0.39-0.97%), Sr (390-1607 ppm) and Ba (330-2500 ppm). They plot within the alkali basalt field on both the TAS and the Nb/Y versus Zr/TiO_2 diagrams (Fig. 5a, b). Nonetheless, on the AFM diagram of Miyashiro (1974) they exhibit a typical tholeiitic trend (Fig. 5c). With decreasing SiO_2, TiO_2, $(Fe_2O_3)^T$, MgO and CaO increase while Al_2O_3 decreases. K_2O, Na_2O and P_2O_5 show no obvious correlation with SiO_2 (Fig. 4).

The Bachu mafic dykes have high total REE abundances (181-477 ppm) with La_N = 7-26. On chondrite-normalized REE plots, they display enriched LREE patterns with relatively constant La_N/Sm_N (2.3-4.4) and Sm_N/Yb_N (3.1-6.6) ratios and insignificant Eu anomalies (δEu = 0.97-1.0) (Fig. 6). Their trace element spider diagram is characterized by significant negative Sr anomalies and negative to positive Ti anomalies, probably due to Ti-bearing magnetite fractionation/accumulation (Fig. 6).

4.2.4 The Halajun granites

The Halajun granite □ and □ are highly silicic in composition with SiO_2 ranges of 71.7% – 75.2 % and 77% – 78.2%, respectively. Their A/CNK values vary between 0.95-1.02, indicating a weak metaluminous to weak peraluminous nature. There is a significant negative correlation between SiO_2 and total alkali (Fig. 5a), suggesting extensive crystal fractionation of alkali feldspar. Probably due to this fractionation, these samples show a sub-alkaline signature (Fig. 5a). However, HFSE may not have been affected by fractionation given their relatively high contents. On the 10000*Ga/Al versus Zr diagram (Fig. 7a), these samples plot in the field of typical A-type granite. Specifically, they show A_1-type characteristics according to the classification of Eby (1992). In this regard, the Halajun granites resemble the syenite plutons and dykes in the Bachu area (Fig. 7b).

The Halajun granite □ and □ have essentially the same trace element compositions except that pluton □ shows more evolved characteristics, with lower δEu and deeper troughs for Ba, Sr, P and Ti than those of the pluton I (Fig. 6). The more evolved nature of pluton □ is also highlighted by its relatively high SiO_2 and low TiO_2, Al_2O_3, Fe_2O_3, CaO, MgO contents compared to pluton □ (Data Repository Table DR2).

4.2.5 The Permian basalts

The Permian basalts have very similar geochemical signatures except that the KF2 samples have higher SiO_2 contents than the KF1 samples. All the samples are characterized by high total alkali (Na_2O+K_2O = 4.15-5.26%) over a relatively narrow SiO_2 range of 44.1-51.2%. They plot within the alkaline basalt field in the TAS diagram (Fig. 5a), consistent with their high Nb/Y ratios (Fig. 5b). Their high $Fe_2O_3^T$ contents show a typical tholeiitic trend in the FeO (t) – Na_2O+K_2O – MgO triangle diagram (Fig. 5c). On the Harker diagrams, Al_2O_3, TiO_2, CaO and MgO increase with decreasing SiO_2, while $Fe_2O_3{}^T$, K_2O, Na_2O and P_2O_5 show more scattered variations (Fig. 4). As for REE and incompatible trace elements, the basalts have high total REE contents (ΣREE = 180-233 ppm) and REE distribution patterns characterized by enriched LREEs and insignificant Eu anomalies (La_N/Yb_N = 6-8, La_N/Sm_N =2.3-2.7, Sm_N/Yb_N = 2.8-3.3, δEu = 0.95-1.0) (Fig. 6). Normalized to primitive mantle, they exhibit coherent incompatible element distribution patterns characterized by positive Ba and negative Sr and Nb (Ta) anomalies (Nb/La = 0.6-0.8, δSr = 0.3-0.5) (Fig. 6).

4.3 Whole-rock Sm-Nd isotopic compositions

The Piqiang samples show variable Sm and Nd contents and $^{147}Sm/^{144}Nd$ ratios (0.1144 - 0.1920). Their $^{143}Nd/^{144}Nd$ ratios range from 0.512436 to 0.512666 and $\varepsilon_{Nd}(t)$ values from -1.05 to 2.08 (Table 1). The Bachu mafic dykes have similar $^{147}Sm/^{144}Nd$ (0.1144 - 0.1262) and high $^{143}Nd/^{144}Nd$ ratios of 0.512524 to 0.512762 ($\varepsilon_{Nd}(t)$ = 0.56 - 5.02). Basaltic samples have consistent $^{147}Sm/^{144}Nd$ and $^{143}Nd/^{144}Nd$ ratios and similar $\varepsilon_{Nd}(t)$ values of -2.05 to -2.57. The Halajun plutons □ and □ have slightly different $\varepsilon_{Nd}(t)$ values, with $\varepsilon_{Nd}(t)$ values for pluton □ averaging ca. -2.0 and pluton □ ca. -0.3. In spite of their different $\varepsilon_{Nd}(t)$ values, the two plutons have similar T_{2DM} (~1.1 Ga) (Table 1).

5. Petrogenesis

5.1 The Piqiang complex

Though the rocks from the Piqiang complex appear to be crystal cumulates, they show enrichments in LREE and LILE (Fig. 6). This, and the $\varepsilon_{Nd}(t)$ range of -1.0 to 2.1, are comparable to some coeval ultramafic-mafic complexes in Tienshan and southern Altay (Han et al., 1999, 2004, 2006; Li et al., 1998; Zhou et al., 2004). Their high Nb/La ratios (mostly >1.0), high-Ti and Fe-rich (*e.g.*, high Fe/Mn ratios of 70-116 and the presence of large magnetite deposits in the Piqiang complex) characteristics argue against a derivation from a recently metasomatized sub-continental lithospheric mantle (SCLM). This is because simple partial melting of metasomatized SCLM could not produce a Fe-rich high-Ti basaltic magma (Baker et al., 1997; Davies and Blanckenburg, 1995; Xu et al., 2001, 2003; Zhang et al., 2009). On the other hand, a sub-lithospheric mantle-derived magma, affected by crustal contamination and crystal fractionation/accumulation, could satisfy the abovementioned elemental and Nd isotopic characteristics. First, the dolerites mingled with the cumulates have trace element characteristics similar to that of OIB despite their having slightly higher Rb, Ba and Th contents and slightly negative Nb (Nb/La = 0.98-1.0) and positive Zr-Hf anomalies (Fig. 6). Second, the weak negative Nb anomaly and higher Th/La and $(Th/Yb)_N$ ratios can be ascribed to crustal contamination. The large range of $\varepsilon_{Nd}(t)$ for the cumulates, and the deviation from the OIB field of some samples in $(Nb/La)_{pm}$ vs. $(Zr/Nd)_{pm}$, Th/Yb vs. Nb/Ta, $(Th/Yb)_N$ vs. $(Nb/Th)_N$ and Th/La vs. Nb/La diagrams (Fig. 8), suggest variable crustal assimilation during magma ascent. Third, the Piqiang complex shares most petrographic, mineralization (large magnetite deposits) and geochemical features with the coeval Wajilitage complex in the Bachu area (Figs. 1 and 2c), which was interpreted as being formed via crystal fractionation/accumulation of an OIB-like primitive magma (Zhang et al., 2008).

The wide ranges of $Mg^{\#}$, MgO, SiO_2 and low values of some compatible trace elements (*e.g.*, Cr < 260 ppm, Ni < 180 ppm) indicate that the Piqiang complex underwent extensive crystal fractionation/accumulation. Negative correlations of SiO_2 with Fe_2O_3 and MgO, and positive correlation between Fe_2O_3 and MgO, point to fractionation of olivine and clinopyroxene (Figs. 5, 8). CaO and Al_2O_3 exhibit more scattered variation while CaO/Al_2O_3 decreases with increasing SiO_2 (Figs. 5, 8). Along with the variable positive Eu and Sr anomalies (Fig. 6), these features are consistent with fractionation/accumulation of plagioclase. Negative P anomalies and positive correlation between P_2O_5 and La indicate fractionation of apatite. In contrast, a significant positive Ti anomaly and deviation from the WPB area to the Ti end in the Ti/100-Zr-Y/3 triangle diagram (Fig. 9) argues for the cumulation of Ti-bearing magnetite. This process may result in the formation of magnetite ore bodies in the complex (Fig. 9).

Crystal fractionation could significantly affect REE and HFSE contents. However, some trace element ratios are insensitive to this process if the paired elements have similar partition coefficients; such ratios can be used to deduce the melting degree and the depth of the primary magma (*e.g.*, Pearce, 2008). In Zr/Nb vs. Ce/Y diagram of Hardarson and Fitton (1991) and the Sm/Yb vs. La/Sm diagram of McKenzie and O'Nions (1991) (Fig. 10), the Piqiang dolerite samples with Nb/La >1.0 plot on the partial melting line of spinel-garnet lherzolite. Taking into account that crustal contamination would have elevated the REE ratios of the dolerites (Sm/Yb and La/Sm ratios of the average continental crust are 2.1 and 11, after Rudnick and Gao, 2003), we infer that the degree of partial melting for the Piqiang complex was greater than 10% (Fig. 10).

5.2 The Bachu mafic dyke swarm

The coherent major and trace element variations for these dykes are consistent with their derivation from a common parental magma. As shown in Figure 8, the less contaminated samples have $(Nb/La)_{pm}$, $(Zr/Nd)_{pm}$, Nb/Ta and Th/Yb ratios similar to those of OIB. In fact, the trace element distribution patterns for the Bachu mafic dykes are strikingly similar to that of OIB. All these features, along with previously reported Nd-Sr isotopic data (Jiang et al., 2004a), indicate a sub-lithospheric mantle source for these dykes (Zhang et al., 2008). Several samples deviate from OIB toward the crustal end members (possibly the lower crust, see the Th/La vs. Nb/La diagram in Fig. 9), indicating variable assimilation of crustal materials.

Their low contents of compatible elements (e.g., Cr <60 ppm, Ni <70 ppm) and MgO ($Mg^{\#}$ = 33-38) suggest that the Bachu mafic dykes have undergone extensive crystal fractionation either in the magma chamber and/or during magma ascent. The decreases in MgO and Fe_2O_3 with increasing SiO_2 (Fig. 5) indicate crystal fractionation of olivine; the negative correlation between SiO_2 and CaO/Al_2O_3 (Fig. 8) suggests the involvement of clinopyroxene fractionation. The variable negative P anomaly and the positive correlation between La and P_2O_5 are consistent with fractionation of apatite (Fig. 8). Decreases in TiO_2 with increasing SiO_2, and the positive or negative Ti anomalies, argue for fractionation/accumulation of Ti-Fe oxides (titanomagnetite), which is confirmed by the presence of Ti-Fe oxides observed in thin sections. Weak Eu anomalies and slight depletion of Sr in trace elements spider diagrams argue for minor crystal fractionation of plagioclase.

Although the Bachu mafic dykes and the Piqiang complex were likely derived from a similar OIB-like mantle source, they have distinguishable geochemical characteristics.

Compared to the Piqiang dolerites, the Bachu mafic dykes are more enriched in LREE than HREE with higher $(La/Yb)_N$ (Fig. 6), have a more alkaline affinity given their higher Nb/Y and Zr/TiO_2 ratios (Fig. 3), and have higher $\varepsilon_{Nd}(T)$ (Table 1). These differences could be attributed to different degrees of partial melting and different amounts of crustal assimilation. Among the Piqiang dolerites, Bachu dolerites and the basalts, the Bachu dolerites have the highest Ti/Y (~500 for Piqiang dolerites, 600-1000 for Bachu dolerites and 400-600 for basalts), $(La/Yb)_N$, $(Sm/Yb)_N$ and Nb/Y ratios. Figure 10 shows that the primitive magma for the Bachu dolerites likely originated from 3~5% partial melting of a garnet-bearing asthenospheric mantle source. In the $(Tb/Yb)_N$ vs. $(Yb/Sm)_N$ diagram (after Zhang et al., 2009, figure not presented), the less contaminated samples plot on the ~5% degree partial melting line of garnet-spinel lherzolite. We thus suggest that the Bachu dolerites formed by ~5% partial melting of a sub-lithospheric mantle source.

5.3 The Halajun A-type granites

Two main models exist for the origin of A-type granites. (1) Fractional crystallization of mafic rocks, with or without substantial assimilation of crustal rocks. This model requires extreme fractionation, which may be possible by magmatic differentiation in one or several, progressively shallower magma chambers, prior to the final emplacement of the magma (Bonin et al., 2004, 2007). (2) Partial melting of pre-existing rocks induced by magmatic underplating. Possible sources of crustal melts include metaigneous or metasedimentary lower or mid-crustal rocks and juvenile mafic underplates (Whalen et al., 1987; Frost et al., 2001; Martin, 2006), variably fractionated and hybridized by repeated injections of mantle magmas.

Partial melting of pre-existing hornblende-bearing calc-alkaline granitoids and metasedimentary rocks (e.g., the Archaean TTG rocks or granulites in Tarim, Hu et al., 2000) at temperatures >900 °C and pressures <4 kbar (*e.g.*, Patiño Douce, 1997) is excluded for the formation of the Halajun granites due to their high Nb/La, low Y/Yb and Yb/Ta ratios and relatively high εNd(T) and juvenile T_{DM} (T_{DM} = 0.9-1.6 Ga and T_{2DM} = 1.1-1.2 Ga , Table 1 and Fig. 11) (Eby, 1990). On the other hand, no mafic microgranitoid enclaves (MME) have been found in the Halajun granites, making the mixing of mantle-derived mafic magma and crustal-derived silicic melts unlikely.

Some A-type intrusions in the Emeishan LIP have been ascribed to the melting products of gabbroic cumulates recently underplated in the lower crust (Luo et al., 2007; Xu et al., 2008), and this model has been supported by experimental work (e.g., Hay and Wendlandt, 1995). The ε_{Nd}(T) values and most geochemical features of the Halajun granites also favor a derivation by melting of a relatively young, juvenile basaltic crustal component (*e.g.,* high Nb/La, low Y/Yb and Yb/Ta ratios, Fig. 11) rather than an early Precambrian mafic lower crust (e.g., Hu et al., 2000). However, several lines of evidence argue against this model. (1) Geochemical modeling shows that Zr vs. Sr and V variations are useful for discriminating between fractional crystallization and melting processes (Peccerillo et al., 2003). Silicic magmas derived from batch melting of mafic rocks generally have Sr >100 ppm and V >50 ppm (Zhong et al., 2007). However, extensive crystal fractionation of a mafic primitive magma could quickly decrease Sr and V contents in the early stage and quickly increase Zr contents in the late stage in the residue melts because of their very different partition coefficients (*i.e.,* D_{Zr} = 0.05; D_V = 4.0; D_{Sr} = 2.5) (Peccerillo et al., 2003). Both plutons □ and □ have very low Sr (<100 ppm for pluton □ and <10 ppm for pluton □) and V (<10 ppm) contents while their Zr ranges from 164 ppm to 367 ppm (Table DR2). Therefore, the silicic magma could not have been generated by a single-stage partial melting of mafic rocks concurrent with crystal fractionation. (2) No inherited zircon cores have been found in CL images and by SHRIMP analyses.

The Halajun A-type granites are spatially, temporally and geochemically closely related to the Piqiang ultramafic-mafic complex. Along the northern margin of Tarim, there are several ca. 275 Ma ultramafic-mafic-(syenites) intrusive complexes and voluminous mafic dykes (Rui et al., 2002; Yang et al., 2007; Zhang et al., 2008; this study). Syenites in the Wajilitage complex were interpreted to be the products of intensive fractionation of OIB-like basaltic magma (Li et al., 2001; Yang et al., 2007; Zhang et al., 2008). As the Halajun granites share very similar geochemical compositions with the syenites in the Wajilitage complex, except that they are more evolved, it is reasonable to suggest that they were the products of intensive fractionation from the same primitive mafic magma as the Piqiang complex and the Bachu mafic dykes, although there exists a clear chemical “Daly gap” between the mafic rocks and the granites. Peccerillo et al. (2003) demonstrated that with a steady fall in temperature, fractioning magmas generally pass rapidly through the intermediate stages, *i.e.*, producing relatively small amounts of intermediate melts. On the other hand, in a fractionating, continuously fed magma chamber, the silicic melts will occupy the top of the reservoir and the mafic magmas will pond at the bottom. The silicic materials sitting at the top of the chamber would be preferentially emplaced into the crust to form

A-type granites, leaving part of the mafic magma at depth and this magma crystallizes to form the mafic to ultramafic cumulates. The presence of strong aero-magnetic anomalies at Atushi, Bachu and Akesu, in combination with the occurrences of ultamafic-mafic complexes and mafic dyke swarms in the Piqiang and Bachu areas, strongly argue for an ultramafic-mafic intrusive belt along the north margin of the Tarim Block (Rui et al., 2002). In constrast to the voluminous mafic rocks along this belt, the volume of granites is relatively small, suggesting that crystal fractionation is a reasonable model because only small amounts of granitic magma could be generated from mafic magmas by intensive fractionation.

A-type granites derived from crystal fractionation of basaltic magma generally have high Zr saturation temperatures (T_{Zr}, *e.g.*, Zhong et al., 2007). The calculated T_{Zr} values for the Halajun plutons □ and □ are 800-830°C and 780-860°C, respectively (after Watson and Harrison, 1983), which are significantly lower than that of basaltic magma-fractionated A-type granites within the Emeishan LIP (Zhong et al., 2007). We note that the Halajun plutons are the products of extreme fractionation. The significant Zr troughs in the trace elements distribution patterns (Fig. 6) indicate zircon crystallization from the magma. However, the coeval syenites at Bachu may represent the least fractionated primary magma for the A-type granites because the Bachu syenites and the Halajun A-type granites share common geochemical signatures (Zhang et al., 2008). T_{Zr} values for the Bachu syenites range from 890°C to 1010°C, consistent with those of basaltic magma-fractionated A-type granites in the Emeishan LIP (Zhong et al., 2007).

The small but distinguishable difference in Nd isotopic compositions between the granites and the Piqiang complex probably resulted from crustal (especially the Archaean crust) contamination during differentiation as negative Nb anomalies have been observed in several samples from this pluton (08KT02-2, 3, 4).

Significant fractional crystallization may have been associated with the formation of the Halajun granites. This is evidenced by the strong depletions in Ba, Sr, P, Ti and Eu as shown in the spider-diagrams and REE patterns (Fig. 6). The course of crystal fractionation from mafic magma to intermediate and then to silicic magma is consistent with that of the syenites in the Wajilitage complex (Zhang et al., 2008). Nevertheless, fractionation of potassic feldspar may have been more prominent than fractionation of plagioclase in the late stage as suggested by the significant Ba depletion, especially for pluton Ⅱ (Fig. 6).

5.4 The Permian basalts

Despite their relatively large SiO_2 range (44.1% to 51.2%), the Permian basalts show a narrow range of REE and trace element compositions (Fig. 6). Their high ratios of Ti/Y (550-660) and La_N/Yb_N (7-8), and negative $\epsilon_{Nd}(t)$ (-2.1 to -2.6), preclude the basalts being derived from a depleted mantle source. Due to their spatial and temporal relationships with the Bachu mafic dyke swarm (Fig. 1), the basalts possibly shared the same asthenospheric mantle source as that of the mafic dykes (Zhou et al., 2009). In this scenario, the negative $\epsilon_{Nd}(t)$ values of the basalts require significant crustal assimilation. However, the low SiO_2 and high MgO (up to 8.0-8.7%), Fe_2O_3 and TiO_2 contents of some analyzed samples (*e.g.*, samples with SiO_2 below 45%) argue against significant addition of crustal material into the primitive magma. Therefore, the negative $\epsilon_{Nd}(t)$ (-2.1 ~ -2.6) values may largely reflect the Nd isotopic compositions of the magma source. A feasible source satisfying all the above elemental and Nd isotopic characteristics is a long-term enriched lithospheric mantle (Farmer et al., 2003; Comin-Chiaramonti et al., 1997; Jiang et al, 2004b). We note that the analyzed samples in this study have moderate negative Nb anomalies (Nb/La = 0.6-0.8), which could have resulted from subduction-related metasomatism during the late Mesoproterozoic to early Neoproterozoic rather than during the Palaeozoic because (1) an active continental margin may have existed along the northern margin of the Tarim Block during the Mesoproterozoic to earliest Neoproterozoic (Liu et al., 1996; Chen et al., 2004; Zhang et al., 2009); (2) during the Palaeozoic, a passive continental margin appears to have persisted along the northern margin of the Tarim Block (see detailed discussions in Rui et al., 2002); and (3) Mesoproterozoic T_{DM} of the basalts (1.3 Ga - 1.5 Ga) may indicate the timing of the metasomatism.

As shown in Figures 5 and 8, Al_2O_3, CaO, MgO and TiO_2 decrease with increasing SiO_2 and MgO and CaO/Al_2O_3 are negatively correlated with Fe_2O_3 and SiO_2, respectively. All these features indicate that olivine and plagioclase, rather than clinopyroxene, were the dominant phases of the crystal fractionation.

The basalts have very coherent Zr/Nb (10-11) and Ce/Y (~2.0) ratios. In the Zr/Nb vs. Ce/Y diagram (Fig. 10a), the basalts plot on the primitive garnet-spinel lherzolite partial melting line with ca. 5-10% melting degrees, which is consistent with the La/Sm vs. Sm/Yb diagram (Fig. 10b). Thus, we conclude that the basalts were derived from 5-10% partial melting of the lower part of a time-integrated enriched lithospheric mantle source and underwent intensive crystal fractionation of olivine and plagioclase.

6. Geodynamic implications

6.1 Age data of the Permian igneous rocks in the Tarim Block

Table 2 lists all the reliable age data for the Permian igneous rocks in the Tarim Block (mostly in northwestern part of Tarim; see Fig. 1). These ages indicate that despite their compositional diversity, all the intrusive rocks (i.e., mafic dykes, ultramafic-mafic complexes, syenite dykes and granites) were formed coevally at *ca.* 275 Ma. Nonetheless, the extrusive rocks display two age peaks, *i.e.*, ca. 290 Ma and ca. 275 Ma. This scenario is similar to that in the Sangtanghu and Tuha basins north of Tienshan (Zhou et al., 2006; Zhang et al., 2010). The age data, in combination with their spatial distribution shown in Figure 1, indicate that the intrusive and extrusive rocks in northern Tarim are temporally and spatially related to each other, with the exception of an earlier phase of basaltic eruptions at ca. 290 Ma, which could be the early phase of the same tectono-magmatic event (see discussions below).

6.2 Lithospheric and sub-lithospheric mantle melting above a common mantle plume

The Early Permian magmatic rocks in the study region display a great variety in lithology and petrology, ranging from ultramafic, basalt, dolerite, syenite to granite and all of them exhibit typical within-plate affinities (Figs. 7c and 9). Despite the different petrogenetic processes associated with them, these diverse rocks share some common features. (1) Except for minor ca. 290 Ma basalts, they were largely emplaced simultaneously at ca. 275 Ma (Table 2). As mentioned above, the two pulses of basalt eruption in Tarim are similar to that in the Tuha and Santanghu basins just north of Tienshan (Fig. 1). According to the regional geology (Xijiang BGMR, 1993; Zhou et al., 2006), the volume of the ca. 290 Ma basalts is much smaller than that of the ca. 275 Ma basalts. Moreover, voluminous mafic dykes, ultramafic-mafic complex, syenite and A-type granites are temporally and spatially related with the ca. 275 Ma basaltic eruptions (Fig. 1). Therefore, we suggest that the Permian igneous activity peaked at ca. 275 Ma after a minor ca. 290 Ma basaltic event that possibly represented the earlier phase of the same Permian igneous activity. (2) the Permian igneous events, with granites, syenites, and ultramafic rocks forming igneous complexes, were closely related in space (Fig. 1). (3) These magmas may have been derived from a common sub-lithospheric source, with the exception of some basalts which may have originated from the lithospheric mantle. It is therefore reasonable to conclude that the generation of these diverse rocks was governed by a common geodynamic process. In particular, such features are typical of large igneous provinces (Coffin and Eldholm, 1994; Bryan and Ernst, 2008; Ernst et al., 2008).

As pointed out by Zhang et al. (2010), geochronological and stratigraphic studies of the Permian basalts in Tarim and surrounding areas show the likely existence of a Permian large igneous province in Tarim and the western part of the CAOB (*i.e.,* the Tarim LIP). This igneous activity would have occurred ca. 15 My before the Emeishan LIP in southwestern China (Zhou et al., 2002, 2008; Xu et al., 2004) and 25 My before the ca. 250 Ma Siberian traps (Reichow et al., 2009). Such a sudden fare up of plume activity in the Permian may represent the early stage of the dipolar Pangean and SW Pacific superplumes due to circum-Pangea subduction and mantle avalanches (Li and Zhong, 2009). The occurrence of diverse igneous rocks during the Permian represents the products of this plume event.

We illustrate in Figure 12 a possible model for the formation of the spatially and temporally related oxide-bearing ultramafic-mafic-(syenite) complexes (e.g., the Piqiang, Wajilitage and Mazaertage complexes), mafic dyke swarms, A-type granites (syenites) and basalts along the northern margin of the Tarim Block, based in part on the ideas developed by Zhou et al. (2008) and Xu et al. (2008) for the deposits and intrusive rocks in the Emeishan LIP. In this model, the Fe-rich magmas that gave rise to the Fe-Ti-rich rocks and their ore deposits were probably derived from a sub-lithospheric mantle source, which was enriched not only in Fe but also in incompatible elements, and most possibly, in volatiles (H_2O and CO_2) (Zhou et al., 2008). Because of the dissolved volatiles, this magma had a relatively low density and passed through the density discontinuities and reached the lower to middle crust. Crystal fractionation in one or several progressively shallowing magma chambers, prior to the final emplacement of the magma, took place during this passage (Bonin et al., 2007). Crystal fractionation produced the magma that was parental to both the Fe-Ti-rich ultramafic complexes and the A-type granites. The formation of the ore minerals was linked to the formation of an unusually Fe-rich magma but the trigger for this process needs further investigation.

Unlike the ultramafic-mafic complexes, the basalts in Tarim were likely derived from partial melting of a time-integrated enriched lithospheric mantle source. The emplacement of enriched CLM-derived magmas before the sub-lithospheric mantle-derived magmatism is consistent with lower melting temperatures of enriched components compared to the “dry” mantle (Turner et al., 1996; Xu, 2001). The trigger for the melting of the enriched CLM components may be related either to convective heating associated with underplating of mafic magmas from the sub-lithospheric mantle, or to conductive heating associated with an upwelling plume and lithospheric thinning. Thus, both the extrusive and intrusive rocks in Tarim could have genetically been related to a Permian upwelling mantle plume (Fig. 12).

7 Conclusions

Based on new data as well as existing information on Permian magmatic activities in Tarim, we draw the following conclusions.

(1) The oxide-bearing ultramafic-mafic-(syenite) complexes (Piqiang, Wajilitage and Mazhaertage), a mafic dyke swarm, and A-type granites were all emplaced at ca. 275 Ma within the interior of the Tarim Block. The voluminous basalts in the Tarim, Jungar, Santanghu and Tuha basins are spatially and temporally related to the intrusive rocks. All these igneous rocks were the likely products of a Permian mantle plume (the Tarim plume). The ca. 290 Ma basaltic eruptions in both the Tarim basin and the region north of Tienshan may represent an earlier phase of the same large igneous event.

(2) Although the intrusive and extrusive rocks are spatially and temporally related to each other, they were derived from different mantle sources. The intrusive rocks and mafic dykes in Tarim were formed via crystal fractionation in one or several, progressively shallowing magma chambers, from a sub-lithospheric mantle-derived primitive basaltic magma. In contrast, the basalts in Tarim were derived from a long-term enriched lithospheric mantle source.

Acknowledgements: We thank Mr. Liu T. for his help during the fieldwork and in providing the 1:5000 geological map of the Wajilitage area. Constructive reviews by Richard Ernst, Mei-Fu Zhou and the chief editor, Prof. Nelson Eby are greatly appreciated. This work was jointly supported by the Natural Science Foundation of China (40721063, 40772123) and the CAS/SAFEA International Partnership Program for Creative Research Teams (KZCX2-YW-t004). This is contribution No. IS-xxxx from GIGCAS, and TIGeR publication #xxx.

References

Arndt, N.T., Chauvel, C., Fedorenko, V., Czamanske, G., 1998. Two mantle sources, two plumbing systems: tholeiitic and alkaline magmatism of the Maymecha River basin, Siberian flood volcanic province. Contribution to Mineralogy and Petrology 133, 297–313.

Arndt, N.T., Czamanske, G.K., Walker, R.J., Chauvel, C., Fedorenko, V.A., 2003. Geochemistry and origin of the intrusive hosts of the Noril'sk–Talnakh Cu–Ni-PGE sulfide deposits. Economic Geology 98, 495–515.

Baker, J.A., Menzies, M.A., Thirwall, M.F., MacPherson, C.G., 1997. Petrogenesis of Quaternary intraplate volcanism; Sana'a; Yemen: implications for plume-lithosphere interaction and polybaric melt hybridization. Journal of Petrology 38, 1359-1390.

Bonin, B., 2004. Do coeval mafic and felsic magmas in post-collisional to within-plate regimes necessarily imply two contrasting, mantle and crustal sources? A review. Lithos 78, 1-24.

Bonin, B., 2007. A-type granites and related rocks: evolution of a concept, problems and prospects. Lithos 97, 1-29.

Borisenko, A.S., Sotnikov, V.I., Izokh, A.E., Polyakov, G.V., Obolensky, A.A., 2006. Permo-Triassic mineralization in Asia and its relation to plume magmatism. Russian Geology and Geophysics 47, 166-182.

Bryan, S.E., Ernst, R.E., 2008. Revised definition of Large Igneous Provinces (LIPs). Earth Science Reviews 86, 175-202.

Campbell, I.H., Czamanske, G.K., Fedorenko, V.A., Hill, R.I., Stepanov, V., 1992.

Synchronism of the Siberian traps and the Permian–Triassic boundary. Science 258, 1760– 1763.

Chen, H. L., Yang, S. F., Wang, Q. H., Luo, J. C., Jia, C. Z., Wei, G. Q., Li, Z. L., 2006. Sedimentary response to the Early-Mid Permian basaltism in the Tarim plate. Geology in China 33, 545-552 (in Chinese with English abstract).

Comin-Chiaramonti, P., Cundari, A., Piccirllo, E.M., Comes, C.B., Castrorina, F., Censi, P., De Min, A., Marzoli, A., Speziale, S., Veldzaccez, V.F., 1997. Potassic and sodic igneous rocks from Eastern Paraguay: their origin from the lithospheric mantle and genetic relationships with the associated Parand flood tholeiites. Journal of Petrology 38, 495-528.

Coffin, M.F., Eldholm, O., 1994. Large igneous provinces: crustal structure, dimension, and external consequences. Review on Geophysics 32, 1-36.

Czamanske, G.K., Zen'ko, T.E., Fedorenko,V.A., Calk, L.C., Budahn, J.R., King, B.S.W., Siems, D.F., 1995. Petrographic and geochemical characterization of ore-bearing intrusions of the Noril'sk-type, Siberia: with discussion of their origin. Resource Geology 18, 1–48.

Davies, J.H., Von Blanckenburg, F., 1995. Slab breakoff: a model of lithosphere detachment and its test in the magmatism and deformation of collisional orogens. Earth and Planetary Science Letters 129, 85–102.

Eby, G.N., 1990. The A-type granitoids: a review of their occurrence and chemical characteristics and speculations on their petrogenesis. Lithos 26, 115-134.

Eby, G..N., 1992. Chemical subdivision of the A-type granitoids: petrogenetic and tectonic implications. Geology 20, 641-644.

Ernst, R.E., Wingate, M.T.D., Buchan, K.L., Li, Z.X., 2008. Global record of 1600–700 Ma Large Igneous Provinces (LIPs): Implications for the reconstruction of the proposed Nuna (Columbia) and Rodinia supercontinents. Precambrian Research 160, 159-178.

Farmer, G. L. 2003. Continental basaltic rocks. In The Crust (ed. Rudnick; R.L.); Vol.3 Treatise on geochemistry (ed. H. D. Holland and K. K. Turekian); Elsevier-Pergamon, Oxford. pp. 85-121.

Fedorenko, V.A., Czamanske, G.K., 1997. Results of new field and geochemical studies of the volcanic and intrusive rocks of the Maymecha–Kotuy area, Siberian flood-basalt province, Russia. International Geology Review 39, 479–531.

Frost, B.R., Barnes, C.G., Collins, W.J., Arculus, R.J., Ellis, D.J., Frost, C.D., 2001. A geochemical classification for granitic rocks. Journal of Petrology 42, 2033-2048.

Hardarson, B.S., Fitton, J.G., 1991. Increased mantle melting beneath Snaefellsjokull volcano during late Pleistocene glaciation. Nature 353, 62–64.

Han, B.F., Ji, J.Q., Song, B., Chen, L. H., Zhang, L., 2006. Late Paleozoic vertical growth of continental crust around the Junger Basin, Xinjiang, China (Part I): timing of post-collisional plutonism: Acta Petrologica Sinica 22, 1077-1086 (in Chinese with English abstract).

Han, B.F., Ji, J.Q., Song, B., Chen, L. H., Li, Z. H., 2004. Zircon SHRIMP U-Pb ages of the Kalatongke and Huangshandong Cu-Ni-bearing ultramafic-mafic intrusions and their geological significances: Chinese Science Bulletin 49, 2324-2328 (in Chinese).

Han, B.F., He, G. Q., Wang, S. G., 1999. Postcollisional mantle-derived magmatism, underplating and implication for the basement of the Jungger Basin: Sciences in China (D-series) 42, 113-119.

Hay D.E., Wendlandt R.F., 1995. The origin of Kenya rift plateau-type flood phonolites—results of high-pressure, high-temperature experiments in the systems phonolite-H_2O and phonolite- H_2O–CO_2. Journal of Geophysical Research-Solid Earth 100(B1), 401–410.

Hu, A.Q., Jahn B.M., Zhang G.X., Zhang Q.F., Chen Y.B., 2000. Crustal evolution and Phanerozoic crustal growth in northern Xinjiang: Nd-Sr isotopic evidence. Part I: isotopic characterisation of basement rocks. Tectonophysics 328, 15-51.

Jiang, C. Y., Jia, C. Z., Li, L. C., Zhang, P. B., Lu, D. R., Bai, K. Y., 2004a. Source of the Fe-enriched-type high –Mg magma in Mazhartag region; Xinjiang. Acta Geologica Sinica 78, 770-780 (in Chinese with English abstract).

Jiang, C. Y., Zhang, P. B., Lu, D. R., Bai, K. Y, Wang, Y. P., Tang, S. H., Wang, J. H., Yang, C., 2004b. Petrology; geochemistry and petrogenesis of the Kalpin basalts and their Nd; Sr and Pb isotopic compositions. Geological Review 50, 492-500 (in Chinese with English abstract).

Li, H., Wang, L.S., Li, C., Liu, S.W., 2005. Experimental study on wave velocity of rocks from Tarim basin at high P-T conditions and its geological implications. Geological Journal of China Universities 11, 601-607 (in Chinese with English abstract).

Li, C. N., Lu, F. X., Chen, M. H., 2001. Research on petrography of the Wajilitag complex body in north edge in the Tarim Basin. Xinjiang Geology 19, 38-42 (in Chinese with

English abstract).

Li, H. Q., Xie, C. F., Chang, H. L., Cai. H., Zhu, J. P., Zhou, S., 1998. Study on the metallogenetic chronology of nonferrous and precious metallic ore deposits in north Xinjiang, China. Beijing: Geological Publishing House, p. 1-250 (in Chinese with English abstract).

Li, Y., Su, W., Kong, P., Zhang, K.Y, Zhang, M.L., Chen, Y., Cai, X.R., Long, D.H., 2007. Zircon LA-ICP-MS ages of the early Permian magmatic rocks in central Tarim and Bachu area. Acta Petrologica Sinica 23, 1097-1107 (in Chinese with English abstract).

Li, X.H., Li, Z.X., Ge, W., Zhou, H., Li, W., Liu, Y., Wingate, M.T.D. 2003. Neoproterozoic granitoids in South China: crustal melting above a mantle plume at ca. 825 Ma? Precambrian Research 122, 45-83.

Li, X.H., Liu, D.Y., Sun, M., Li, W.X., Liang, X.R., Liu, Y., 2004. Precise Sm-Nd and U-Pb isotopic dating of the super-giant Shizhuyuan polymetallic deposit and its host granite; Southeast China. Geological Magazine 141, 225-231.

Li, X.H., Li, Z.X., Zhou, H., Liu, Y., Peter, D. K., 2002. U-Pb zircon geochronology; geochemistry and Nd isotopic study of the Neoproterozoic biomodal volcanic rocks in the Kangdian rift of South China: implication for the initial rifting of Rodinia: Precambrian Research 113, 135-154.

Li, Z.X., Bogdanova, S.V., Collins, A.S., Davidson, A., De Waele, B., Ernst, R.E., Fitzsimons, I.C.W., Fuck, R.A., Gladkochub, D.P., Jacobs, J., Karlstrom, K.E., Lu, S., Natapov, L.M., Pease, V., Pisarevsky, S.A., Thrane, K., Vernikovsky, V., 2008. Assembly; configuration; and break-up history of Rodinia: A synthesis. Precambrin

Research (doi:10.1016/j.precamres.2007.04.021).

Li, Z.X., Zhong, S., 2009. Supercontinent–superplume coupling, true polar wander and plume mobility: Plate dominance in whole-mantle tectonics: Physics of the Earth and Planetary Interiors 176, 143-156.

Lu, S. N., Li, H. K., Zhang, C. L., Niu, G. H., 2008. Geological and geochronological evidence for the Precambrian evolution of the Tarim craton and surrounding continental fragments. Precambrian Research 160, 94-107.

Luo Z. Y., Xu Y. G., He B., Shi Y. R. and Huang X. L., 2007. Geochronologic and petrochemical evidence for the genetic link between the Maomaogou nepheline syenites and the Emeishan large igneous province. Chinese Science Bulletin 52, 949–958.

Ludwig, K.R., 1999. Using Isoplot/EX, version 2, a geolocronolgical Toolkit for Microsoft Excel. Berkeley Geochronological Center Special Publication 1a, 47.

Ludwig, K.R., 2001, Squid 1.02: a user manual. In: Berkeley Geochronological Center Special Publication l2, p. 19.

Mao, J.W., Pirajno, F., Zhang, Z.H., Chai, F.M., Chen, S.P., Yang, M.J., Zhang, C.Q., 2008. A review of the Cu–Ni sulphide deposits in the Chinese Tianshan and Altay orogens (Xinjiang Autonomous Region, NW China): Principal characteristics and ore-forming processes. Journal of Asian Earth Sciences 32, 184-203.

Martin, R.F., 2006. A-type granites of crustal origin ultimately result from open-system fenitization-type reactions in an extensional environment. Lithos 91, 125-136.

McKenzie, D.P., Bickle, M. J., 1988. The volume and composition of melt generated by extension of the lithosphere. Journal of Petrology 29, 625-679.

McKenzie, D.P., O'Nions, R.K., 1991. Partial melt distributions from inversion of rare earth element concentrations. Journal of Petrology 32, 1021–1091.

Miyashiro, A., 1974. Volcanic rock series in island arcs and active continental margins. American Journal of Science 274, 321-355.

Patiño Douce, A.E., 1997. Generation of metaluminous Atype granites by low pressure melting of calcalkaline granitoids. Geology 25, 743–746.

Peccerillo, A., Barberio, M.R., Yirgu, G., Ayalew, D., Barbieri, M., Wu, T.W., 2003. Relationships between mafic and peralkaline silicic magmatism in continental rift settings: a petrological, geochemical and isotopic study of the Gedemsa Volcano, central Ethiopian rift. Journal of Petrology 44, 2003-2032.

Pearce, J.A., Cann, J.R., 1973. Tectonic setting of basic volcanic rocks determined using trace element analyses. Earth and Planetary Science Letters 19, 290–300.

Pearce, J.A., Thirlwall, M.F., Ingram, G., Murton, B.J., Arculus, R.J., Van der Laan, S.R., 1992. Isotopic evidence for the origin of Boninites and related rocks drilled in the Izu-Bonin (Ogasawara) forearc, Leg 125. In: Fryer, P., Pearce, J.A., Stokking, L. (Eds.), Proceedings of the Ocean Drilling Program. Scientific Results 125, 237-261.

Pearce, J.A., 2008. Geochemical fingerprinting of oceanic basalts with applications to ophiolite classification and the search for Archean oceanic crust. Lithos 100, 14-48.

Pirajno, F., Mao, J.W., Zhang, Z.C., Zhang, Z.H., Chai, F.M., 2008. The association of mafic–ultramafic intrusions and A-type magmatism in the Tian Shan and Altai orogens, NW China: Implications for geodynamic evolution and potential for the discovery of new ore deposits. Journal of Asian Earth Sciences 32, 165-183.

Pirajno,F., Ernst, R.E., Borisenko, A.S., Fedoseev, G.., Naumov, E.A., 2009. Intraplate magmatism in central Asia and China and associated metallogeny. Ore Geology Reviews 35, 114-136.

Polyakov, G.V., Izokh, A.E., Borisenko, A.S., 2008. Permian ultramafic-mafic magmatism and accompanying Cu-Ni mineralization in the Gobi-Tien Shan belt as a result of the Tarim plume activity. Russian Geology and Geophysics 49, 455-467.

Reichow, M.K., Pringle, M.S., Al'Mukhamedov, A.I., Allen, M.B., Andreichev, V.L., Buslov, M.M., Davies, C.E., Fedoseev, G.S., Fitton, J.G., Inger, S., Medvedev, A.Y.,Mitchell, C., Puchkov, V.N., Safonova, I.Yu., Scott, R.A., Saunders, A.D., 2009. The timing and extent of the eruption of the Siberian Traps large igneous province: implications for the end-Permian environmental crisis. Earth and Planetary Science Letters 277, 9-20.

Rudinick, R.L., Gao, S., 2003. Composition of the continental crust. In: Holland, H.D., and Turekian, K.K. (ed.): Treatise on geochemistry. Elsevier-Pergamon, Oxford. 1-64.

Rui, X. J., He, J. R., Guo, K. Y., 2002. Mineral resources of Tarim Block (in Chinese); Beijing: Geological Publishing House: 56-157 (in Chinese with English abstract).

Sun, S.S. and McDonough, W.F., 1989. Chemical and isotopic systematics of oceanic basalt: implication for mantle composition and processes. In: Saunders A.D. and Norry M.J. (ed.); Magmatism in the ocean basin. Geological Society of London Special Publication 42, 528-548.

Stacey, J.S., Kramers, J.D., 1975. Approximation of terrestrial lead isotope evolution by two-stage model. Earth and Planetary Science Letters 26, 207-221.

Tian, W., Campbell, T.H., Allen, C., Guan, P., Pan, W.Q., Chen, M.M., Yu, H.J., Zhu, W.P.,

2010. The Tarim picrite–basalt–rhyolite suite, a Permian flood basalt from northwest China with contrasting rhyolites produced by fractional crystallization and anatexis DOI 10.1007/s00410-009-0485-3

Turner, S., Hawkesworth, C.J., Gallagher, K., 1996. Mantle plumes, flood basalts, and thermal models for melt generation beneath continents: assessment of a conductive heating model and application to the Parana. Journal of Geophysics Research 101, 11503-11518.

Wang, C.Y., Zhou, M.F., Zhao, D.G., 2008. Fe–Ti–Cr oxides from the Permian Xinjie mafic–ultramafic layered intrusion in the Emeishan large igneous province, SW China: Crystallization from Fe- and Ti-rich basaltic magmas. Lithos 102, 198-217.

Wang, X.C., Li, X.H., Li, W.X., Li, Z.X., 2009. Variable involvements of mantle plumes in the genesis of mid-Neoproterozoic basaltic rocks inSouth China: A review. Gondwana Research 15, 381-395.

Wang, L.S., Li, C., Li, F.T., 1996. Thermal-rheological structure of the lithosphere beneath two types of basins in eastern and western China. Science in China (ser. D) 30, 116-121.

Watson, E.B., Harrison, T.M., 1983. Zircon saturation revisited: temperature and composition effects in a variety of crustal magma types. Earth and Planetary Science Letters 64, 295－304.

Whalen, J.B.; Currie, K.L.; Chappell, B.W., 1987. A-type granites: geochemical characteristics; discrimination and petrogenesis. Contribution to Mineralogy and Petrology 95, 407-419.

Winchester, J.A., Floyd, P.A., 1977. Geochemical discrimination of different magma series and their differentiation products using immobile elements. Chemical Geology 20, 325-343.

Williams, I.S., 1998. U-Th-Pb geochronology by ion microprobe. Reviews on Economic Geology 7, 1-35.

Xu, J.F., Shinjo, R., Defant, M.J., Wang, Q., Rapp, R.P., 2002. Origin of Mesozoic adakitic intrusive rocks in the Ningzhen area of east China: partial melting of delaminated lower continental crust? Geology 30, 1111–1114.

Xinjiang, BGMR., 1993. Regional Geology of the Xinjiang Uygur Autonomous Region: Beijing; Geological Publishing House. 2-145 (in Chinese).

Xu, Y.G., 2001 Thermo-tectonic destruction of the Archaean lithospheric keel beneath eastern China: evidence, timing and mechanism. Physics and Chemistry of the Earth (A), 26: 747-757

Xu, Y.G., Chung, S.L., Jahn, B.M., Wu, G.Y., 2001, Petrological and geochemical constraints on the petrogenesis of the Permo-Triassic Emeishan flood basalts in southwestern China. Lithos 58, 145–168.

Xu, Y. G., He, B., Chung, S.L., Menzies, M.A., Frey, F.A., 2004. Geological, geochemical and geophysical consequences of plume involvement in the Emeishan flood-basalt province. Geology 32, 917–920.

Xu Y. G., He B., 2007. Thick and high velocity crust in Emeishan large igneous province, SW China: evidence for crustal growth by magmatic underplating/intraplating. In The Origins of Melting Anomalies. Plates, Plumes, and Planetary Processes, vol. 430 (eds. G.

Foulger and D. Jurdy). Geological Society of America Special Publication, pp. 841–858.

Xu, Y. G., Luo, Z.Y., Huang, X.L., He, B., Xiao, L., Xie, L.W., Shi, Y.R., 2008. Zircon U-Pb and Hf isotope constraints on crustal melting associated with the Emeishan mantle plume. Geochimica et Cosmochimica Acta 72, 3084-3104.

Yang, S. F., Chen, H. L., Dong, C. W., 1995. The discovery of the Permian syenite inside of Tarim Basin and its geodynamic significance. Geochemica 25, 121-128 (in Chinese).

Yang, S. F., Chen, H. L., Ji, D. W., Li, Z. L., Dong, C. W., Jia, C. Z., Wei, G. Q., 2005. Geological process of early to middle Permian magmatism in Tarim Basin and its geodynamic significance. Geology Journal of Chinese University 11, 504-511 (in Chinese).

Yang, S. F., Li, Z. L., Chen, H. L., Xiao, W. J., Yu, X., Lin, X. W., Shi, X. G., 2006. Discovery of a Permian quartz syenite porphyritic dyke from the Tarim Basin and its tectonic implications. Acta Petrologica Sinica. 22, 1405-1412 (in Chinese with English abstract).

Yang, S.F., Li, Z.L., Chen, H.L., Santosh, M., Dong, C.W., Yu, X., 2007. Permian bimodal dyke of Tarim Basin; NW China: Geochemical characteristics and tectonic implications. Gondwana Research doi:10.1016/j.gr.2007.10.018.

Zhong, H., Zhu, W.G., Chu, Z.Y., He, D.F., Song, X.Y., 2007. Shrimp U-Pb zircon geochronology, geochemistry, and Nd-Sr isotopic study of the contrasting granites in the Emeishan large igneous province, SW China. Chemical Geology 236, 112-133.

Zhou, M.F., Malpas, J., Song, X.Y, Kennedy, A.K., Robinson, P.T., Sun, M., Lesher, C.M., Keays, R.R., 2002. A temporal link between the Emeishan large igneous province (SW

China) and the end- Guadalupian mass extinction. Earth and Planetary Science Letters 196, 113-122.

Zhou, M.F., Lesher, C.M., Yang, Z.X., Li. J.W., Sun, M., 2004. Geochemistry and petrogenesis of 270 Ma Ni–Cu–(PGE) sulfide-bearing mafic intrusions in the Huangshan district; Eastern Xinjiang; Northwest China: implications for the tectonic evolution of the Central Asian orogenic belt. Chemical Geology 209, 233-257.

Zhou, M.F., Arndt, N.T., Malpas, J., Wang, C.Y., Kennedy, A.K., 2008. Two magma series and associated ore deposits types in the Permian Emeishan large igneous province, SW China. Lithos 103, 352-368.

Zhou, M.F., Zhao, J.H., Jiang, C.Y., Gao, J.F., Wang, W., Yang, S.H., 2009. OIB-like, heterogeneous mantle sources of Permian basaltic magmatism in the western Tarim Basin, NW China: Implications for a possible Permian large igneous province. Lithos 113, 583-594.

Zhou, D. W., Liu, Y. Q., Xin, X. J., Hao, J. R., Dong, Y. P., Ouyang, Z. J., 2006. Tracing and reconstruction of the Palaeo tectonic background of the Permian basalts in Tuha and Sangtanghu Basins, NW China. Science in China (D series), 26, 143-153.

Zhang, C.L., Li, X.H., Li, Z.X., Lu, S.N., Ye, H. M., Li, H. M., 2007. Neoproterozoic ultramafic-mafic-carbonatite complex and granitoids in Quruqtagh of northeastern Tarim Block, western China: geochronology, geochemistry and tectonic implications. Precambrian Research 152, 149-169.

Zhang, C. L., Li, X. H., Li, Z. X., Ye, H. M., Li, C. N., 2008. A Permian layered intrusive complex in the western Tarim Block, northwestern China: product of a ca.275 Ma mantle plume? Journal of Geology 116, 112-128.

Zhang, C.L., Li, Z.X., Li, X.H., Ye, H.M., 2009. Neoproterozoic mafic dyke swarms in northern margin of the Tarim Block: Age, geochemistry and implications on the breakup of Rodinia. Journal of Asian Earth Sciences 35, 167-179.

Zhang, C.L., Li, Z.X., Li, X.H., Xu, Y.G., Zhou, G., Ye, H.M., 2010. A Permian large igneous province in Tarim and Central Asian Orogenic Blet (CAOB), NW China: Results of a ca. 275 Ma mantle plume? Geological Society of America Bulletin (doi: 10.1130/B30007.1).

Zhang, Z.C., Mao, J.W., Saunders, A.D., Ai, Y., Li, Y., Zhao, L., 2009. Petrogenetic modeling of three mafic–ultramafic layered intrusions in the Emeishan large igneous province, SW China, based on isotopic and bulk chemical constraints. Lithos 113, 369-392.

Fig Captions

Fig. 1 A geotectonic sketch map of the Tarim Block and part of the Central Asian Orogenic Belt (CAOB) in Xinjiang, showing the distribution of the Permian basalts, ultamafic-mafic intrusions, mfic dykes and A-type granites, with their ages shown in Ma (grey, blue and blank stars represent the locations of dated mafic-ultramafic intrusions, basalts and mafic dykes, and granitic intrusions, respectively). Insert in the lower-left corner shows the locations of the CAOB and the main crustal blocks to the north and south of the CAOB. The locations of the studied Piqiang complex, Halajun granite plutons, Bachu mafic dyke swarm, and basalts are shown. Discussions about the dividing line between the two mantle provinces (or domains) can be found in Zhang et al. (2010). KF1 – the Kupukuziman Formation at the Yingan section; KF2 – the Kapaizileike Formation at the Kaipaizileike section; M – the Mazaertage complex; W – the Wajilitage complex; P – the Piqiang complex.

Fig. 2 (a) Simplified geological map of the Piqiang complex and the Halajun granite plutons (plutons I and II); (b) detailed geological map of part of the Piqiang complex showing the rock types of the complex; (c) detailed geological map of the mafic dyke swarm around the Wajilitage complex showing the broadly radiating distribution (based on the 1:5000 geological mapping by local geologists).

Fig. 3 Concordia plots of U-Pb zircon results of the studied intrusive rocks: (a) the Piqiang complex, (b) the Halajun granite pluton □, (c) - the Halajun granite pluton □.

Fig. 4 Binary Harker diagrams (SiO_2 versus Al_2O_3, TiO_2, Fe_2O_3, CaO, MgO, Na_2O, K_2O, P_2O_5 and Zr versus Rb, V, La and Nb) for the Piqiang complex, Bachu mafic dyke swarm and basalts (see detailed discussion in the text).

Fig. 5 SiO_2 vs.$K_2O + Na_2O$ (a) and Nb/Y vs. Zr/TiO_2 (b) classification diagrams (after Floyd et al., 1977) and AFM (Na_2O+K_2O – FeO^T –MgO) diagram (c) showing the tholeiitic trends of the Piqiang complex, the Bachu mafic dyke swarm and the Permian basalts (FeO^T=$Fe_2O_3{}^T$/1.111).

Fig. 6 Chrondrite-normalized REE patterns and primitive mantle-normalized incompatible element spider-diagrams for the studied rocks. The normalization values are from Sun and McDonough (1989).

Fig. 7 Zr vs 10000Ga/Al discrimination diagram showing that the intermediate and felsic sub-groups from the Halajun granite plutons are A-type granites (after Whalen et al., 1987), where I = I-type, S = S-type and M = M-type granitoids (a); Nb-Y-Ce discrimination diagram indicating A_1 characteristics of the Halajun granite plutons (after Eby, 1992) (b) and Y vs. Nb diagram showing their typical within-plate chemical characteristics (c) (see detailed discussions in the text).

Fig. 8 Binary Harker diagrams for rocks of the Piqiang intrusive complex, Bachu mafic dykes and basalts. PM – primitive mantle, UC – upper crust, MC – middle crust, LC – lower crust, OIB – oceanic island basalt, N-MORB – normal middle ocean ridge basalt (see details in the text).

Fig. 9 Ti/100 – Zr – Y*3 triangle diagram showing the typical intraplate geochemical signatures of the Piqiang complex, the Bachu mafic dykes, and the basalts (after Pearce and Cann, 1973).

Fig. 10 Ce/Y vs. Zr/Nb (a) and La/Sm vs. Sm/Yb (b) plots of the Piqiang mafic dykes, less contaminated Bachu mafic dykes and basalts along the northern margin of Tarim. Mantle compositions: GD—depleted garnet lherzolite; GP—primitive garnet lherzolite; SD—depleted spinel lherzolite; SP—primitive spinel lherzolite. Numbers on lines refer to percentages of melt (after Hardarson and Fitton, 1991; McKenzie and O'Nions, 1991).

Fig. 11 A Y/Yb vs. Yb/Ta diagram showing that the Halajun A-type granites plot in the OIB –like mafic magma source (after Eby, 1990).

Fig. 12 A generalized model for the two magma series and associated ore deposit types within the Tarim LIP, NW China.

Figure 1

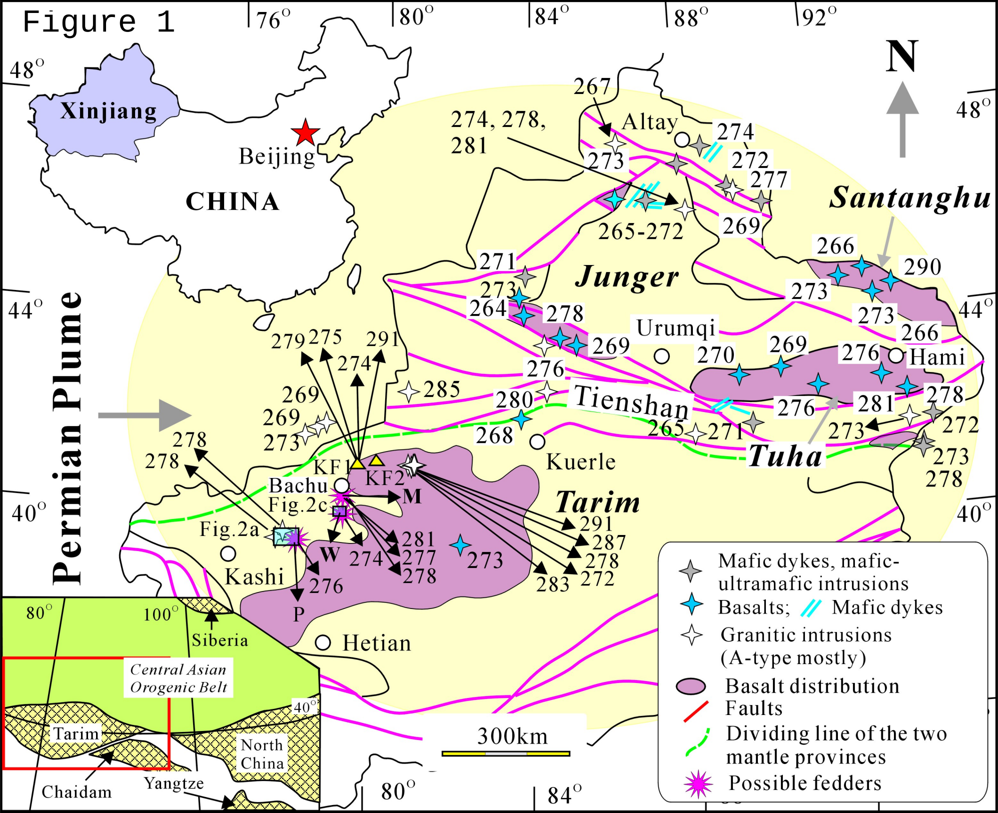

Xinjiang
Beijing
CHINA
Permian Plume
Altay
Junger
Santanghu
Urumqi
Hami
Tienshan
Tuha
Kuerle
Tarim
Bachu
Fig.2c
Fig.2a
KF1
KF2
M
W
P
Kashi
Hetian
300km
Siberia
Central Asian Orogenic Belt
Tarim
North China
Chaidam
Yangtze
Mafic dykes, mafic-ultramafic intrusions
Basalts; Mafic dykes
Granitic intrusions (A-type mostly)
Basalt distribution
Faults
Dividing line of the two mantle provinces
Possible fedders

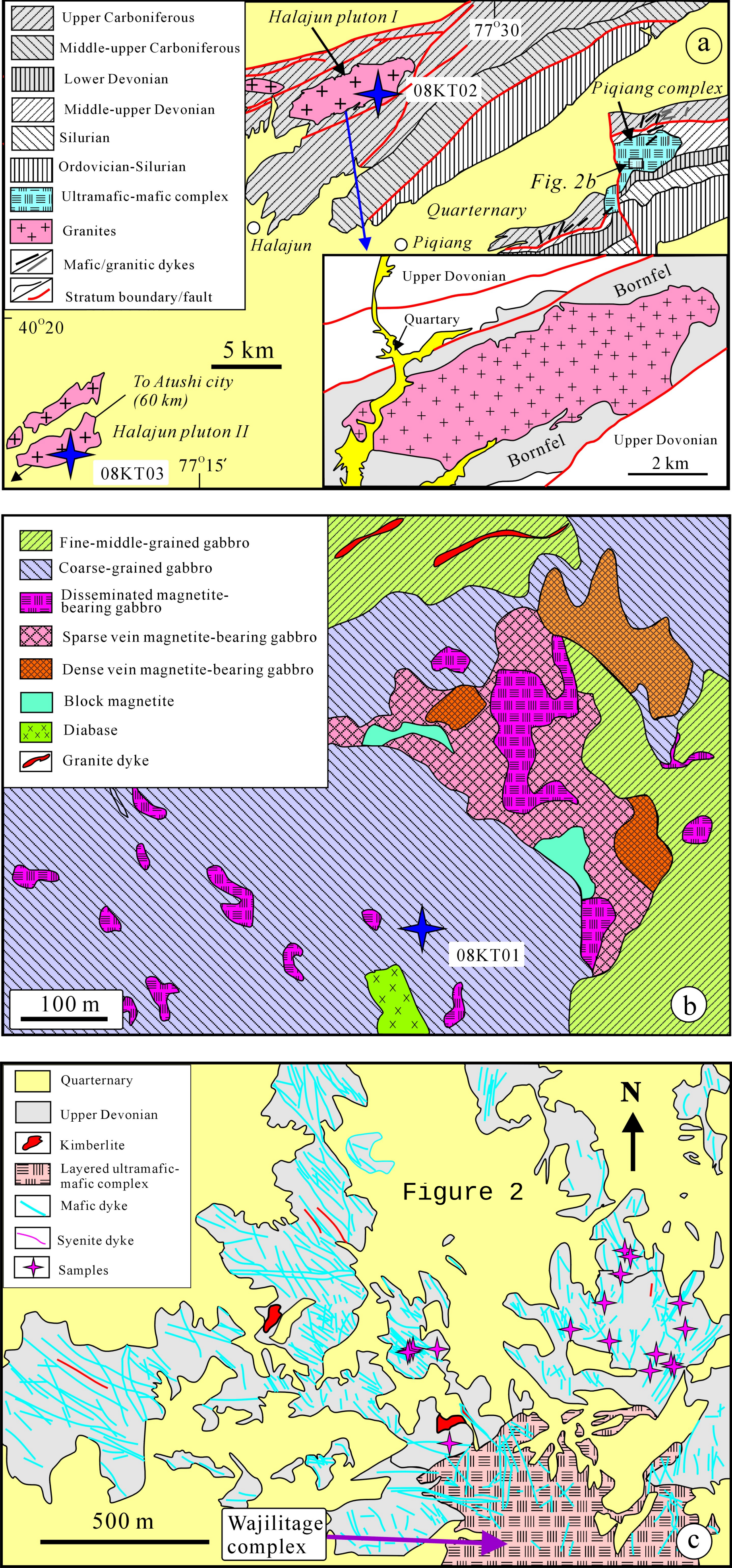

Upper Carboniferous
Middle-upper Carboniferous
Lower Devonian
Middle-upper Devonian
Silurian
Ordovician-Silurian
Ultramafic-mafic complex
Granites
Mafic/granitic dykes
Stratum boundary/fault
Halajun pluton I
77°30
a
08KT02
Piqiang complex
Fig. 2b
Quarternary
Halajun
Piqiang
40°20
5 km
To Atushi city
(60 km)
Halajun pluton II
08KT03
77°15′
Upper Dovonian
Bornfel
Quartary
Bornfel
Upper Dovonian
2 km
Fine-middle-grained gabbro
Coarse-grained gabbro
Disseminated magnetite-bearing gabbro
Sparse vein magnetite-bearing gabbro
Dense vein magnetite-bearing gabbro
Block magnetite
Diabase
Granite dyke
08KT01
100 m
b
Quarternary
Upper Devonian
Kimberlite
Layered ultramafic-mafic complex
Mafic dyke
Syenite dyke
Samples
N
Figure 2
500 m
Wajilitage complex
c

Fig. 3

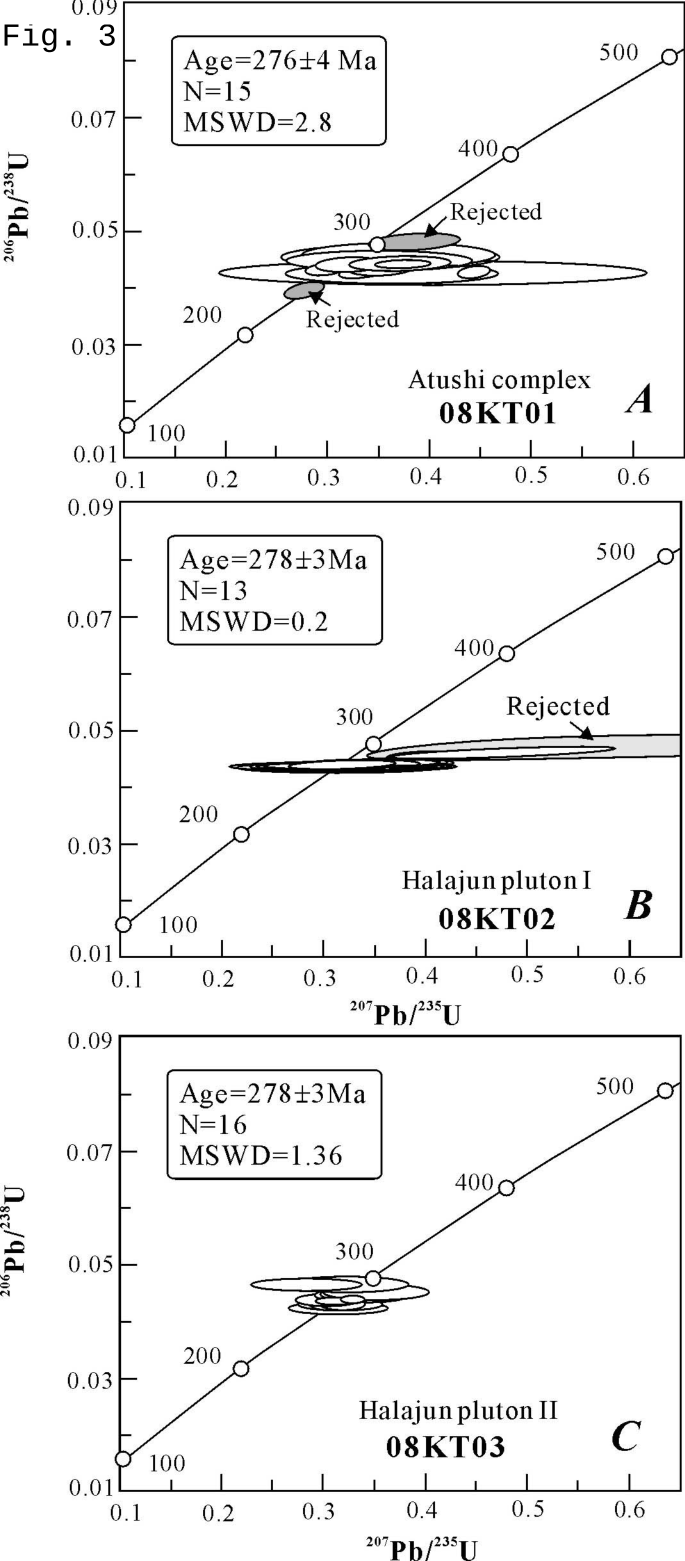

Age=276±4 Ma
N=15
MSWD=2.8
500
400
300
200
100
Rejected
Rejected
Atushi complex
08KT01
A
0.09
0.07
0.05
0.03
0.01
0.1
0.2
0.3
0.4
0.5
0.6
$^{206}Pb/^{238}U$
Age=278±3Ma
N=13
MSWD=0.2
500
400
300
200
100
Rejected
Halajun pluton I
08KT02
B
0.09
0.07
0.05
0.03
0.01
0.1
0.2
0.3
0.4
0.5
0.6
$^{207}Pb/^{235}U$
Age=278±3Ma
N=16
MSWD=1.36
500
400
300
200
100
Halajun pluton II
08KT03
C
0.09
0.07
0.05
0.03
0.01
0.1
0.2
0.3
0.4
0.5
0.6
$^{206}Pb/^{238}U$
$^{207}Pb/^{235}U$

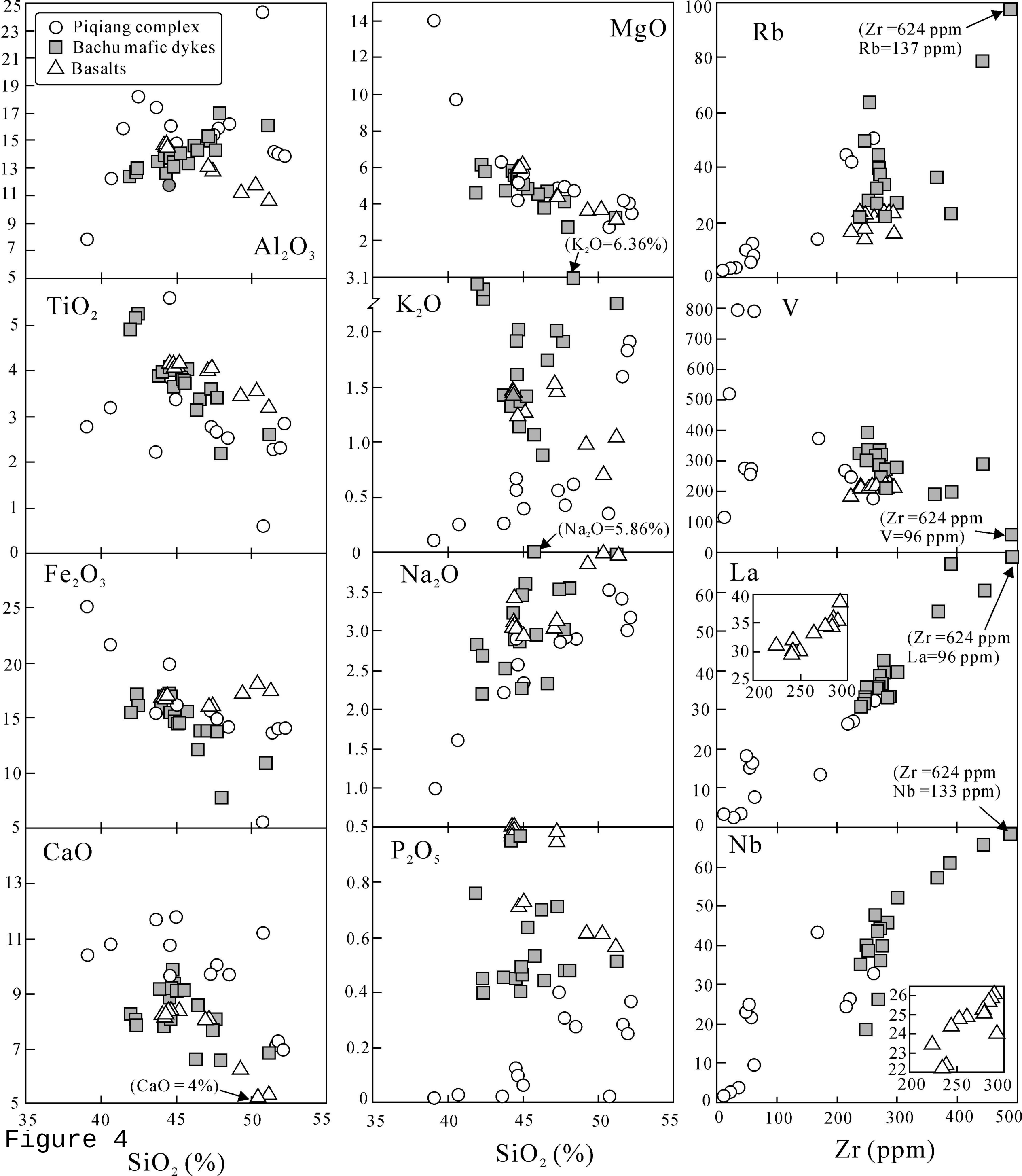

Piqiang complex
Bachu mafic dykes
Basalts
Al2O3
MgO
Rb
(Zr =624 ppm Rb=137 ppm)
(K2O=6.36%)
TiO2
K2O
V
(Na2O=5.86%)
(Zr =624 ppm V=96 ppm)
Fe2O3
Na2O
La
(Zr =624 ppm La=96 ppm)
(Zr =624 ppm Nb =133 ppm)
CaO
P2O5
Nb
(CaO = 4%)
SiO2 (%)
SiO2 (%)
Zr (ppm)

Figure 4

Figure 5

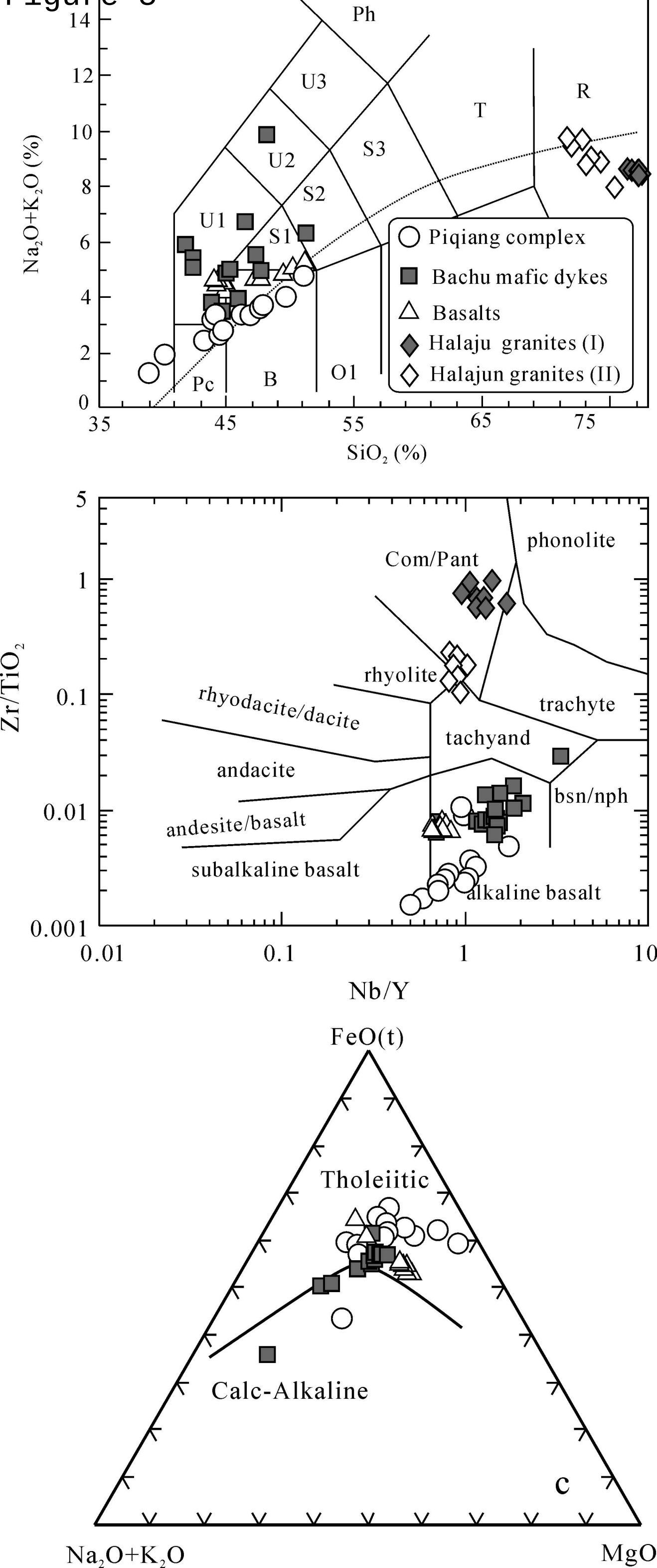

Ph
U3
U2
U1
S3
S2
S1
T
R
Pc
B
O1
Na2O+K2O (%)
SiO2 (%)
Piqiang complex
Bachu mafic dykes
Basalts
Halaju granites (I)
Halajun granites (II)
phonolite
Com/Pant
rhyolite
rhyodacite/dacite
trachyte
tachyand
andacite
bsn/nph
andesite/basalt
subalkaline basalt
alkaline basalt
Zr/TiO2
Nb/Y
FeO(t)
Tholeiitic
Calc-Alkaline
c
Na2O+K2O
MgO

Figure 6

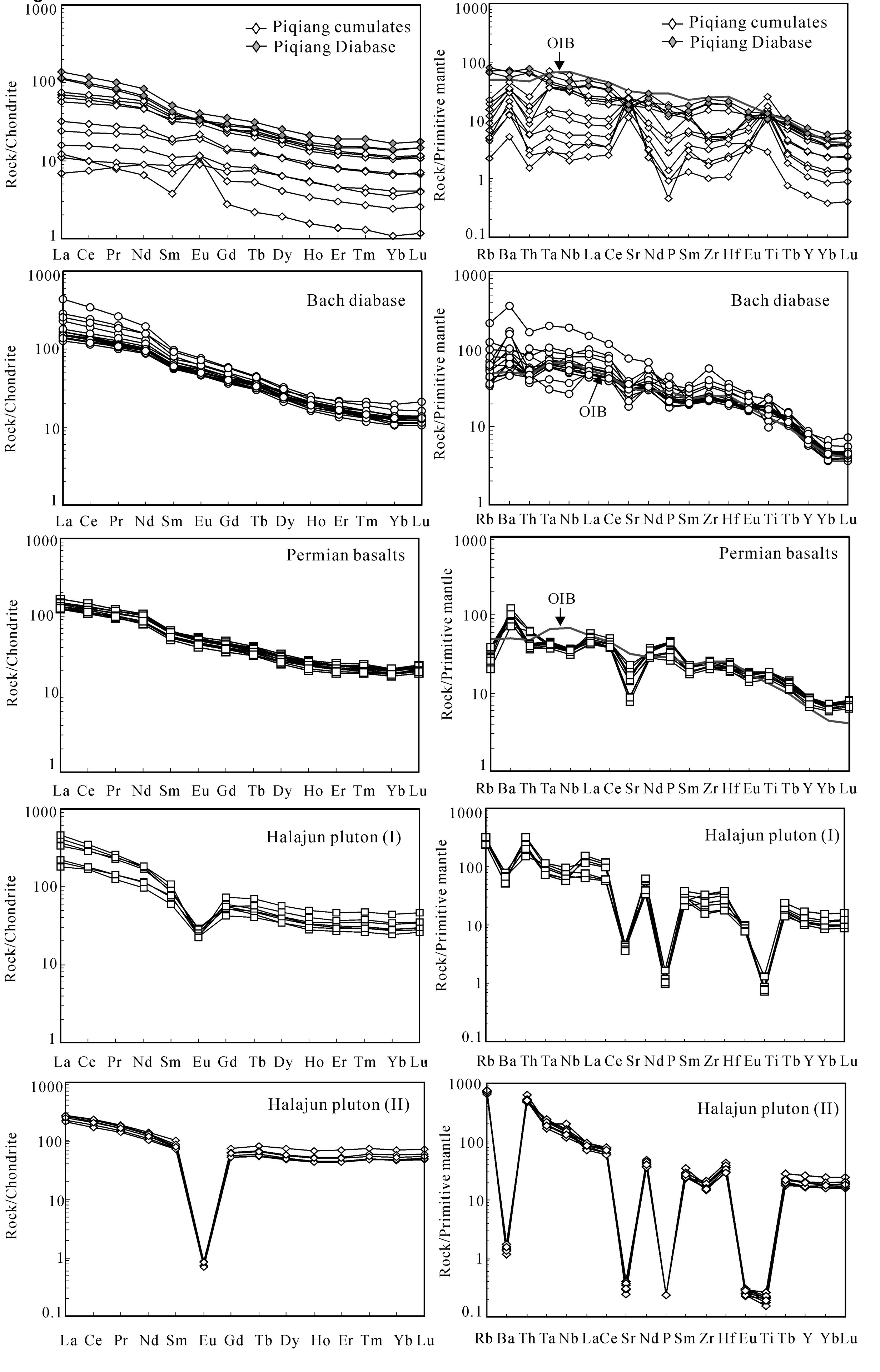
Piqiang cumulates
Piqiang Diabase
OIB
Bach diabase
Permian basalts
Halajun pluton (I)
Halajun pluton (II)
Rock/Chondrite
Rock/Primitive mantle
La Ce Pr Nd Sm Eu Gd Tb Dy Ho Er Tm Yb Lu
Rb Ba Th Ta Nb La Ce Sr Nd P Sm Zr Hf Eu Ti Tb Y Yb Lu
1000
100
10
1
0.1

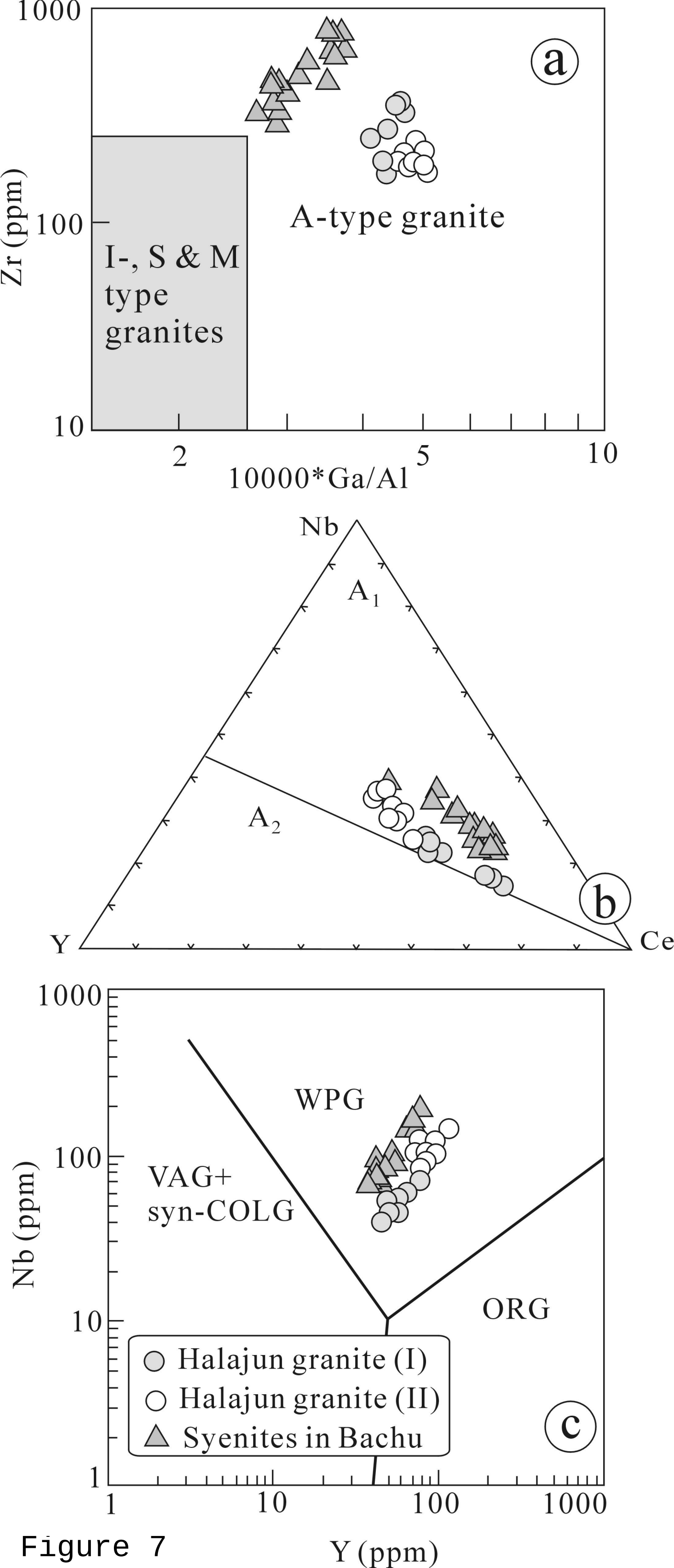
1000
100
10
Zr (ppm)
2
5
10
10000*Ga/Al
a
A-type granite
I-, S & M
type
granites
Nb
Y
Ce
A1
A2
b
1000
100
10
1
Nb (ppm)
1
10
100
1000
Y (ppm)
WPG
VAG+
syn-COLG
ORG
c
Halajun granite (I)
Halajun granite (II)
Syenites in Bachu

Figure 7

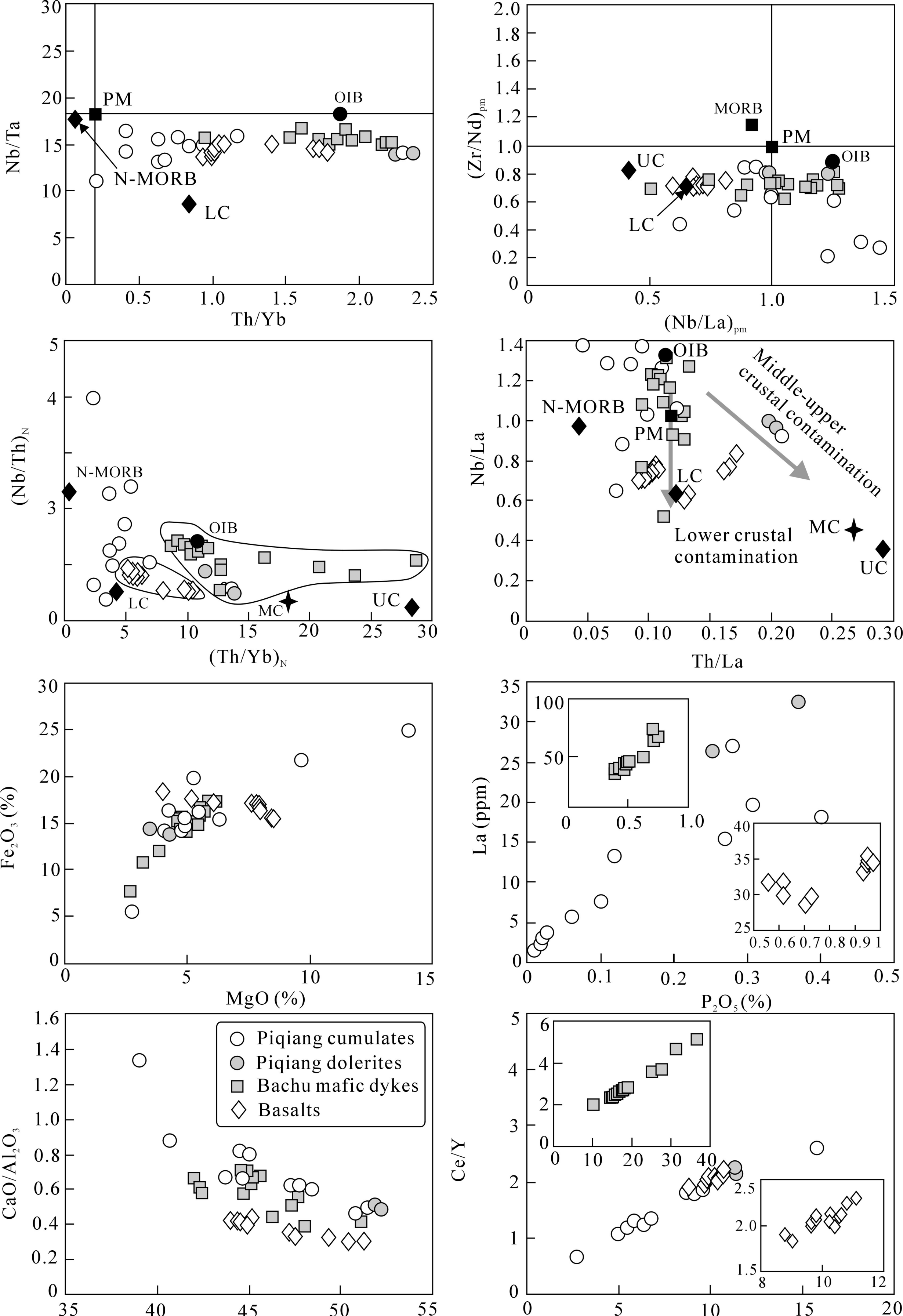
Nb/Ta
Th/Yb
PM
OIB
N-MORB
LC
(Zr/Nd)pm
(Nb/La)pm
MORB
PM
OIB
UC
LC
(Nb/Th)N
(Th/Yb)N
N-MORB
OIB
LC
MC
UC
Nb/La
Th/La
OIB
N-MORB
PM
LC
Middle-upper crustal contamination
Lower crustal contamination
MC
UC
Fe2O3 (%)
MgO (%)
La (ppm)
P2O5 (%)
CaO/Al2O3
SiO2 (%)
Piqiang cumulates
Piqiang dolerites
Bachu mafic dykes
Basalts
Ce/Y
La/Yb

Figure 8

Figure 9

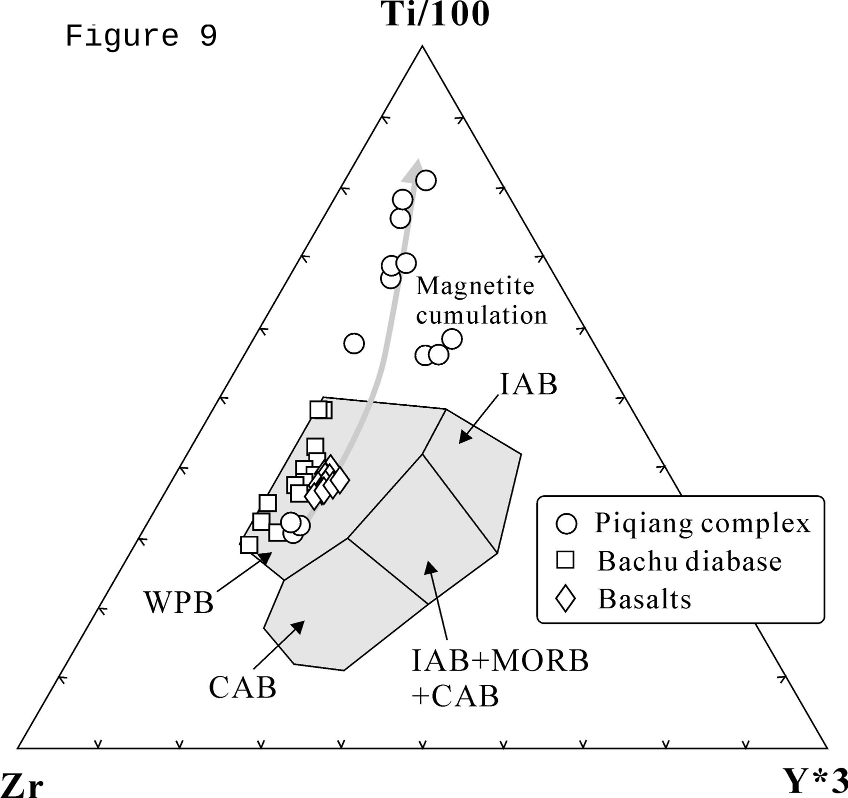

Ti/100
Magnetite
cumulation
IAB
WPB
CAB
IAB+MORB
+CAB
Piqiang complex
Bachu diabase
Basalts
Zr
Y*3

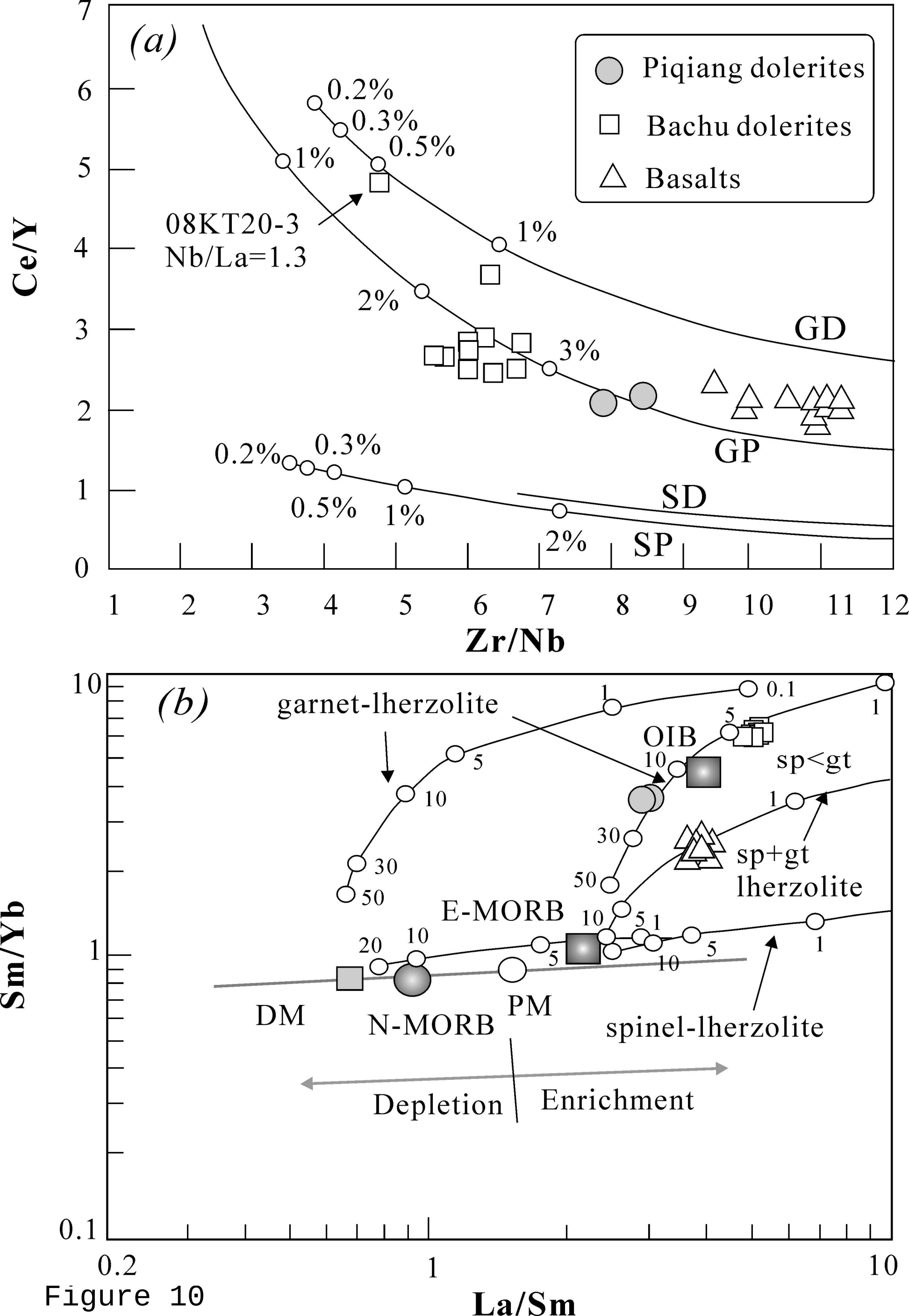
(a)
Piqiang dolerites
Bachu dolerites
Basalts
Ce/Y
Zr/Nb
08KT20-3
Nb/La=1.3
GD
GP
SD
SP
0.2%
0.3%
0.5%
1%
2%
3%
(b)
garnet-lherzolite
OIB
sp<gt
sp+gt
lherzolite
E-MORB
DM
N-MORB
PM
spinel-lherzolite
Depletion
Enrichment
Sm/Yb
La/Sm

Figure 10

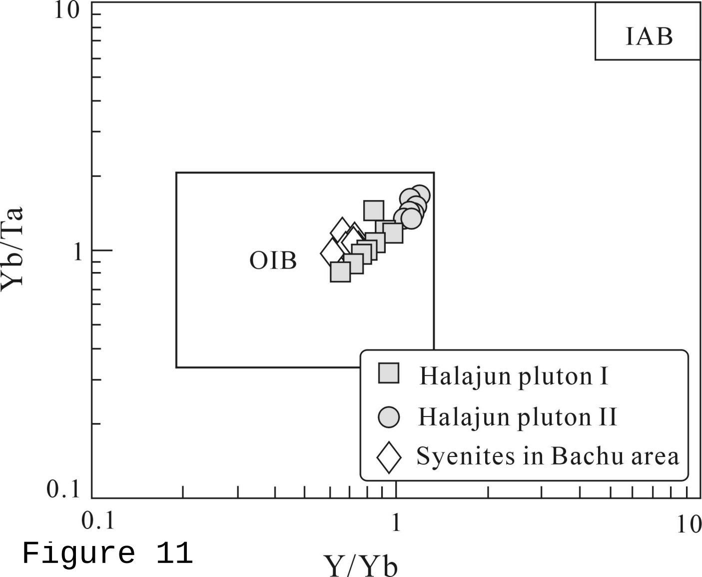
10
1
0.1
Yb/Ta
IAB
OIB
Halajun pluton I
Halajun pluton II
Syenites in Bachu area
0.1
1
10
Y/Yb
Figure 11

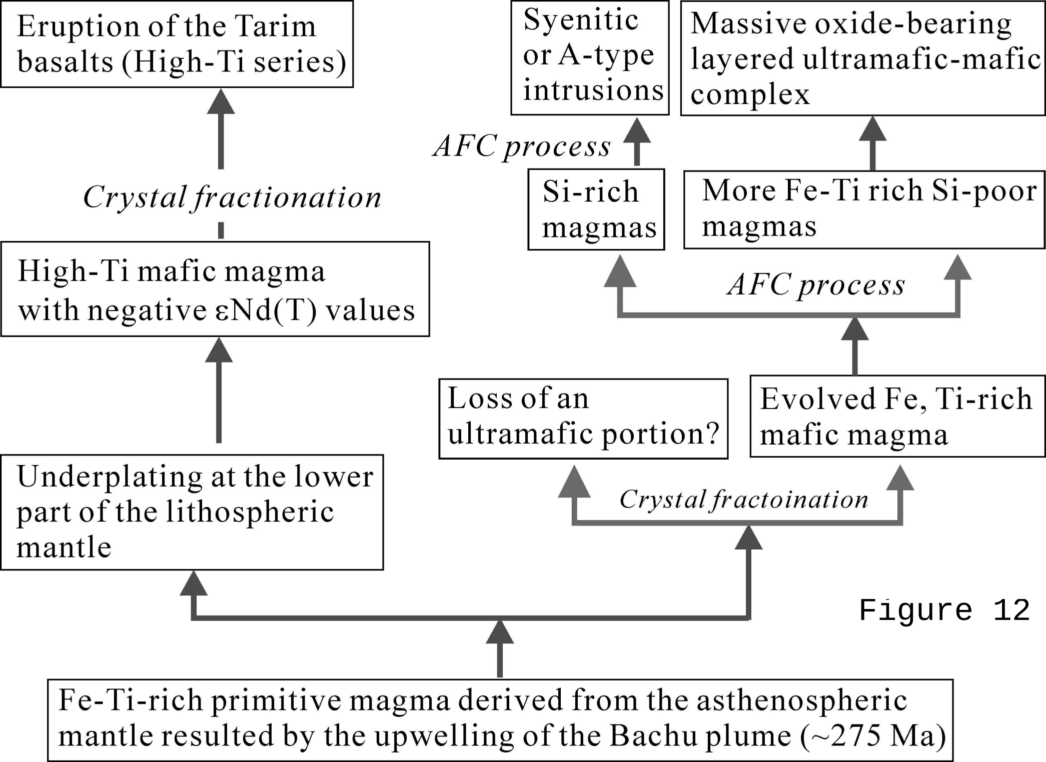
Eruption of the Tarim basalts (High-Ti series)
Crystal fractionation
High-Ti mafic magma with negative εNd(T) values
Underplating at the lower part of the lithospheric mantle
Syenitic or A-type intrusions
Massive oxide-bearing layered ultramafic-mafic complex
AFC process
Si-rich magmas
More Fe-Ti rich Si-poor magmas
AFC process
Loss of an ultramafic portion?
Evolved Fe, Ti-rich mafic magma
Crystal fractoination
Fe-Ti-rich primitive magma derived from the asthenospheric mantle resulted by the upwelling of the Bachu plume (~275 Ma)

Figure 12

Table.1 SHRIMP U-Pb data for zircons from the Piqiang complex and Halajun granits

Spot	U (ppm)	Th (ppm)	Th/U	f_{206}# (%)	$^{206}Pb^*/^{238}U$ (±1σ%)		$^{207}Pb^*/^{235}U$ (±1σ%)		$^{207}Pb^*/^{206}Pb^*$ (±1σ%)		$^{206}Pb/^{238}U$ Age (Ma) (±1σ)		$^{207}Pb/^{206}Pb$ Age (Ma)(±1σ)	
Piqing ultramafic-mafic complex (08KT01)														
1.1	148	74	0.51	2.24	.0440	2.1	0.48	11.4	0.0785	11.2	307.6	4.9	530	210
2.1	180	121	0.70	4.42	.0437	1.3	0.34	2.7	0.0558	2.4	296.9	4.4	536	178
3.1	172	70	0.42	1.72	.0438	1.5	0.49	8.0	0.0808	7.9	272.3	4.1	316	287
4.1	61	36	0.60	4.08	.0467	1.9	0.38	20.7	0.0587	20.6	277.3	5.6	1160	223
5.1	254	246	1.00	0.77	.0434	1.3	0.30	4.1	0.0505	3.9	276.0	3.6	446	53
6.1	160	136	0.88	0.85	.0442	1.3	0.30	4.2	0.0494	4.1	276.6	4.2	1216	155
7.1	94	73	0.80	2.63	.0456	1.7	0.41	14.0	0.0648	13.9	294.1	5.6	554	449
8.1	455	524	1.19	1.65	.0438	1.6	0.37	8.1	0.0617	7.9	274.1	3.4	220	90
9.1	531	211	0.41	1.58	.0455	1.4	0.30	9.2	0.0478	9.1	279.0	3.4	165	95
10.1	115	59	0.53	0.76	.0403	1.3	0.28	5.7	0.0509	5.6	287.2	4.9	768	293
11.1	120	59	0.51	1.71	.0451	1.6	0.42	15.1	0.0682	15.0	276.6	4.3	662	169
12.1	234	225	0.99	2.28	.0435	1.6	0.41	12.0	0.0681	11.9	287.0	4.0	89	215
13.1	452	329	0.75	6.97	.0436	3.7	0.41	42.3	0.0686	42.1	255.0	3.2	238	129
14.1	150	78	0.54	2.24	.0440	2.1	0.48	11.4	0.0785	11.2	284.1	4.5	875	311
15.1	139	112	0.83	0.42	.0437	1.3	0.34	2.7	0.0558	2.4	274.5	4.4	870	246
16.1	62	39	0.66	1.72	.0438	1.5	0.49	8.0	0.0808	7.9	275.2	10.1	887	870
17.1	128	93	0.75	2.64	.0439	1.8	0.30	14.7	0.0494	14.6	276.9	4.9	169	342
18.1	168	88	0.54	0.75	.0440	1.6	0.37	5.2	0.0614	5.0	277.8	4.3	654	107
Halajun granite (pluton Ⅰ, 08KT02)														
1.1	80	44	0.56	2.6	.0460	3.8	0.58	29.6	0.0917	29.3	289.8	10.9	1461	557
2.1	112	56	0.51	1.0	.0434	1.6	0.30	20.4	0.0500	20.3	273.8	4.2	197	472
3.1	145	80	0.57	0.9	.0446	1.3	0.33	14.3	0.0532	14.3	281.3	3.4	338	323
4.1	90	34	0.39	1.1	.0458	1.7	0.48	19.7	0.0757	19.6	288.4	4.8	1088	393
5.1	109	61	0.58	1.0	.0435	1.8	0.32	26.7	0.0539	26.7	274.8	4.8	367	601
6.1	169	64	0.39	0.8	.0438	1.0	0.31	11.2	0.0510	11.2	276.4	2.8	239	258
7.1	155	86	0.57	1.3	.0444	1.5	0.34	11.1	0.0558	11.0	279.8	4.1	443	245
8.1	122	84	0.71	0.9	.0443	1.3	0.32	20.2	0.0530	20.1	279.4	3.6	329	457
9.1	109	73	0.69	1.0	.0436	1.5	0.30	25.8	0.0503	25.8	275.0	4.0	207	598
10.1	146	95	0.67	0.8	.0436	1.5	0.35	18.2	0.0587	18.2	275.2	3.9	556	396
11.1	115	78	0.70	1.4	.0442	1.7	0.33	15.7	0.0534	15.6	278.8	4.6	344	353
12.1	129	79	0.63	0.9	.0427	1.0	0.32	11.6	0.0537	11.6	269.6	2.8	359	261
13.1	118	80	0.70	2.46	.0442	2.3	0.33	14.7	0.0547	14.5	278.6	6.2	400	324
14.1	146	94	0.67	1.20	.0450	2.2	0.37	9.9	0.0589	9.6	284.0	6.0	565	210
Halajun granite (pluton Ⅱ, 08KT03)														
1.1	840	217	0.27	0.12	.0922	1.9	0.74	2.3	0.0584	1.2	569.1	10.7	546	25

2.1	188	80	0.44	0.48	.0439	2.1	0.36	4.5	0.0600	4.0	274.1	5.6	604	87
3.1	115	78	0.70	0.99	.0453	2.2	0.40	9.9	0.0648	9.6	281.0	6.3	767	203
4.1	270	91	0.35	0.29	.0449	2.0	0.37	4.1	0.0599	3.6	280.7	5.6	601	77
5.1	506	233	0.48	0.42	.0438	2.0	0.45	4.3	0.0738	3.9	269.0	5.3	1037	78
6.1	239	104	0.45	0.26	.0443	2.0	0.39	4.1	0.0645	3.5	275.3	5.5	758	74
7.1	80	30	0.39	1.11	.0431	2.4	0.48	10.3	0.0808	10.0	262.7	6.1	1216	197
8.1	197	88	0.46	0.65	.0452	2.0	0.44	7.3	0.0704	7.0	278.5	5.8	939	143
9.1	132	53	0.42	0.51	.0457	2.1	0.47	7.4	0.0745	7.1	280.5	6.0	1055	144
10.1	213	99	0.48	0.12	.0427	2.0	0.41	5.1	0.0688	4.7	263.8	5.4	894	98
11.1	240	94	0.41	0.14	.0432	2.0	0.41	2.9	0.0694	2.1	266.9	5.3	912	43
12.1	235	116	0.51	0.17	.0424	2.0	0.35	3.0	0.0594	2.2	265.2	5.3	580	49
13.1	115	46	0.41	0.64	.0432	2.1	0.45	9.2	0.0753	8.9	265.1	6.0	1076	179
14.1	260	112	0.45	0.10	.0448	2.0	0.41	6.6	0.0665	6.3	277.6	5.7	823	131
15.1	211	95	0.46	0.17	.0433	2.0	0.43	7.3	0.0713	7.1	266.8	5.6	965	144
16.1	160	86	0.55	0.00	.0457	2.1	0.49	7.7	0.0772	7.4	279.2	6.1	1126	147
17.1	340	140	0.43	0.00	.0437	2.0	0.39	6.8	0.0644	6.5	271.7	5.5	756	136

f_{206}: percentage of common ^{206}Pb in total ^{206}Pb

Table 2 Chemical compositions of the Permian ultramafic-mafic complex, mafic dyke swarm, basalts and granites along the northern margin of the Tarim Block

sample	08KT 01-1	08KT 01-2	08KT 01-3	08KT 01-5	08KT 01-6	08KT 01-8	08KT 01-9	08KT 01-10	08KT 01-11	08KT 01-12	08KT 01-13	08KT 01-14	08KT 01-15
Rock type	MGB	PGB	MQGB	MGB	QGB	OMGB	MGB	MQGB	MGB	MGB	MQGB	DB	DB
Major elements (%)													
SiO_2	43.63	50.75	47.72	40.63	51.89	39.08	44.97	48.43	44.55	44.58	47.33	51.56	52.18
TiO_2	2.22	0.62	2.65	3.17	2.33	2.77	3.37	2.53	5.57	3.82	2.75	2.28	2.85
Al_2O_3	17.38	24.33	15.91	12.27	14.06	7.77	14.71	16.23	11.74	16.10	15.43	14.13	13.91
Fe_2O_3	15.39	5.52	14.89	21.62	14.06	25.04	16.18	14.10	19.81	16.28	15.68	13.87	14.29
MnO	0.12	0.05	0.17	0.18	0.16	0.24	0.16	0.16	0.22	0.14	0.18	0.14	0.19
CaO	11.65	11.19	10.02	10.80	7.21	10.41	11.83	9.75	9.66	10.74	9.69	7.06	6.91
MgO	6.28	2.73	4.90	9.63	4.13	14.02	5.60	4.71	5.27	4.23	4.89	4.24	3.50
K_2O	0.26	0.35	0.42	0.25	1.83	0.11	0.40	0.61	0.67	0.57	0.55	1.60	1.91
Na_2O	2.23	3.52	2.91	1.62	3.01	1.01	2.36	2.90	2.57	2.94	2.87	3.40	3.17
P_2O_5	0.02	0.02	0.31	0.03	0.25	0.01	0.06	0.28	0.12	0.10	0.40	0.28	0.37
LOI	0.33	0.33	0.31	0.55	0.71	0.73	0.04	0.10	0.49	0.08	0.15	1.09	0.39
Σ	99.5	99.4	100.2	100.8	99.7	101.2	99.7	99.8	100.7	99.57	99.92	99.64	99.67
$Mg^{\#}$	41	45	36	43	33	49	37	36	31	30	34	34	29
Trace elements (ppm)													
La	2.62	2.91	16.54	3.81	26.46	1.65	5.71	15.5	13.39	7.67	18.1	27.1	32.4
Ce	6.08	6.07	40.0	9.37	57.8	4.55	14.0	36.5	33.1	18.3	43.2	60.8	72.4
Pr	0.89	0.74	5.61	1.40	7.48	0.79	2.13	5.13	4.83	2.60	6.14	7.91	9.47
Nd	4.19	3.06	25.1	6.47	30.6	4.22	10.01	22.3	21.8	12.02	26.9	32.13	38.9
Sm	1.06	0.58	5.40	1.66	6.20	1.34	2.67	4.85	5.18	2.91	5.79	6.49	7.88
Eu	0.68	0.64	1.95	0.68	1.87	0.52	1.10	1.73	2.08	1.26	2.02	1.90	2.36
Gd	1.13	0.56	5.15	1.72	5.84	1.48	2.82	4.68	5.11	2.92	5.40	6.08	7.27
Tb	0.20	0.08	0.82	0.30	0.96	0.28	0.47	0.76	0.91	0.50	0.86	0.99	1.18
Dy	1.04	0.48	4.43	1.63	5.08	1.60	2.79	4.11	4.83	2.73	4.66	5.40	6.51
Ho	0.19	0.09	0.80	0.31	0.97	0.30	0.53	0.75	0.91	0.50	0.85	0.98	1.20
Er	0.49	0.23	2.06	0.74	2.56	0.76	1.34	1.98	2.42	1.30	2.20	2.57	3.14
Tm	0.07	0.03	0.30	0.11	0.38	0.10	0.19	0.28	0.37	0.18	0.31	0.38	0.48
Yb	0.41	0.18	1.81	0.69	2.32	0.60	1.17	1.78	2.30	1.12	1.91	2.39	2.87
Lu	0.07	0.03	0.29	0.10	0.37	0.10	0.17	0.27	0.37	0.18	0.29	0.37	0.45
Rb	2.79	3.07	5.62	3.22	44.63	1.43	4.29	12.08	14.16	7.59	9.72	41.98	50.62
Ga	20.3	21.0	20. 8	18.4	21.7	14.2	20.2	19.8	20.7	24.5	21.1	21. 7	23.4
V	522	113	270	796	265	841	961	260	377	786	269	247	176
Cr	103	17.6	16.5	260	3.02	195	171	15.8	0.41	72.5	17.5	3.67	0.53
Ni	93.1	39.7	33.4	173	23.0	163	43.8	32.1	18.3	42. 5	34.4	27.6	0.07
Sc	27.0	5.54	22.8	35.2	21.8	44.9	39.9	21.0	38.1	30.6	23.1	21.4	22.0
Sr	491	653	527	310	369	235	415	502	384	491	506	322	391
Ba	88.4	147	225	85.3	506	36.5	122	239	314	206	243	375	467
Th	0.26	0.22	0.75	0.47	5.47	0.13	0.49	1.50	2.15	0.86	1.21	5.51	6.45
U	0.06	0.06	0.33	0.09	1.12	0.07	0.10	0.33	0.42	0.19	0.30	1.17	1.49
Ta	0.21	0.12	1.52	0.30	1.75	0.13	0.52	1.48	2.90	0.62	1.50	1.87	2.37
Nb	2.70	1.88	24. 8	3.92	24.5	1.45	7.35	21.9	43.1	9.71	23.3	26.5	32.8

Zr	22.0	11.2	56.3	35.2	215	18.5	51.2	57.9	168	62.4	46.9	221	259
Hf	0.76	0.33	1.57	1.22	5.70	0.69	1.53	1.64	4.40	1.96	1.45	5.74	6.58
Y	4.90	2.35	22.5	7.92	25.7	7.02	13.1	20.3	25.2	13.4	23.6	27.2	33.2

sample	08KT 13-1	08KT 16-1	08KT 16-2	08KT 16-3	08KT 17-1	08KT 18-1	08KT 18-9	08KT 19-1	08KT 19-2	08KT 19-3	08KT 19-4	08KT 19-5	08KT 20-1	08KT 20-2	08KT 20-3	08KT 21-1
Rock type	DB	DB	DB	DB	DB	DB	DB	DB	DB	DB	DB	DB	DB	DB	DB	DB
Major elements (%)																
SiO_2	44.60	47.2	43.79	47.68	44.79	51.14	42.29	45.72	44.49	45.21	44.87	42.35	46.27	47.99	41.89	44.78
TiO_2	4.05	3.59	3.87	3.41	4.02	2.59	5.15	4.01	3.83	3.81	3.98	5.22	3.12	2.15	4.89	3.63
Al_2O_3	14.04	14.95	13.65	14.26	13.21	16.05	13.04	13.34	12.43	14.22	13.52	13.15	14.68	16.94	12.40	13.67
Fe_2O_3	17.21	13.90	15.70	13.9	16.7	10.89	17.22	15.76	15.66	14.38	15.12	16.10	12.10	7.64	15.45	14.69
MnO	0.20	0.18	0.19	0.17	0.17	0.14	0.20	0.19	0.15	0.19	0.17	0.17	0.18	0.05	0.15	0.16
CaO	8.06	7.68	9.11	8.06	9.22	6.89	8.01	9.11	8.81	9.09	9.30	7.69	6.50	6.49	8.20	9.83
MgO	5.74	4.92	4.64	4.15	5.54	3.16	6.07	4.59	5.59	4.88	5.14	5.69	3.79	2.70	4.61	5.41
K_2O	1.61	2.01	1.42	1.91	1.13	2.25	2.96	1.07	1.92	1.42	1.37	2.73	0.88	6.36	3.05	2.02
Na_2O	2.88	3.52	2.51	3.00	2.29	3.98	2.20	2.96	2.90	3.61	3.45	2.69	5.86	3.54	2.81	2.94
P_2O_5	0.97	0.71	0.45	0.48	0.41	0.51	0.39	0.53	0.45	0.63	0.50	0.45	0.70	0.48	0.76	0.47
LOI	0.15	0.82	4.31	2.56	2.08	1.94	2.01	2.32	3.33	2.05	2.16	3.30	5.73	5.20	5.38	1.92
Σ	99.60	99.5	99.64	99.59	99.59	99.55	99.54	99.58	99.55	99.49	99.58	99.55	99.81	99.55	99.58	99.51
$Mg^{\#}$	36	37	33	33	36	33	37	33	38	36	36	37	35	37	33	38
Trace elements (ppm)																
La	33.5	54.8	36.0	39.1	30.0	39.1	33.0	39.6	36.1	42.5	35.7	35.8	67.2	103	60.1	32.4
Ce	76.8	116.8	81.4	86.7	69.3	86.3	75.0	89.8	83.6	96.4	81.0	80.7	147	207	133	74.6
Pr	10.6	15.0	10.8	11.3	9.45	11.2	10.0	12.1	11.2	13.0	10.9	10.7	19.1	25.0	17.8	10.2
Nd	45.7	60.4	45.4	47.5	40.5	46.4	42.1	51.0	47.4	54.2	46.8	44.4	73.9	91.7	73.8	44.0
Sm	9.28	11.44	9.25	9.37	8.46	9.02	8.61	10.4	9.64	10.6	9.71	8.88	12.5	15.0	14.0	9.10
Eu	2.84	3.65	2.94	2.91	2.70	2.75	2.68	3.23	2.96	3.29	3.15	2.74	3.55	4.45	4.18	2.86
Gd	8.68	10.1	8.47	8.21	7.55	7.95	7.36	9.23	8.53	9.23	8.84	7.88	9.93	12.0	11.7	8.17
Tb	1.36	1.45	1.27	1.24	1.16	1.19	1.11	1.37	1.26	1.39	1.32	1.18	1.33	1.68	1.64	1.24
Dy	7.39	6.98	6.43	6.17	5.83	5.97	5.43	6.82	6.34	6.75	6.51	5.81	6.28	8.23	7.89	6.17
Ho	1.36	1.13	1.10	1.08	1.01	1.02	0.91	1.19	1.08	1.18	1.13	0.96	1.07	1.40	1.28	1.07
Er	3.59	2.62	2.64	2.69	2.54	2.61	2.25	2.99	2.67	2.87	2.81	2.38	2.66	3.47	3.13	2.72
Tm	0.53	0.35	0.36	0.38	0.35	0.35	0.30	0.41	0.37	0.41	0.38	0.33	0.37	0.49	0.41	0.37
Yb	3.32	1.94	2.11	2.25	1.95	2.13	1.80	2.39	2.10	2.33	2.27	1.85	2.14	2.83	2.37	2.20
Lu	0.54	0.29	0.31	0.35	0.29	0.33	0.27	0.35	0.31	0.34	0.34	0.29	0.32	0.41	0.35	0.33
Rb	34.0	36.9	33.1	37.3	21. 7	44.7	63.6	27.1	39.8	22.7	27.3	50.5	22.9	137	78.1	28.2
Ga	21.6	25.4	25.1	23.6	23.4	24.0	22.6	24.4	23.1	24.0	24.8	22.9	23.7	24.6	25.6	23.2
V	212	199	307	243	326	287	392	278	318	272	328	338	211	96	290	298
Cr	59.4	0.42	0.16	0.33	12.4	12.7	4.90	1.80	21.4	34.7	14.4	0.03	5.10	21.8	1.10	12.8
Ni	67.4	12.4	23.5	17.9	58.2	38.7	38.2	18.8	49.6	48.5	53.5	15.1	14.4	13.8	31.5	56.9
Sc	23.4	16.8	23.4	20.3	24.9	25.0	27.5	19.9	24.9	24.5	24.0	23.3	15.3	3.9	17.6	24.0
Sr	388	700	593	646	534	618	633	572	642	672	729	455	637	1607	806	750
Ba	1187	696	555	660	505	110	664	327	422	457	332	542	318	2496	719	449
Th	3.15	6.97	4.12	4.94	3.50	4.70	3.64	4.54	3.89	4.01	3.64	4.02	8.70	13.9	6.71	3.35
U	0.72	1.72	1.03	1.09	0.82	1.00	0.96	1.03	1.00	1.20	0.94	1.06	2.60	2.83	1.60	0.82
Ta	1.66	2.47	3.06	2.63	2.35	2.36	2.54	3.15	2.85	2.94	2.62	1.24	3.79	8.22	4.30	2.44
Nb	25.8	57.1	47.3	40.2	35.0	36.0	39.8	52.2	44.4	45.6	43.7	18.7	61.1	133	65.6	38.5

Zr	281	366	264	274	239	270	251	299	270	278	266	249	388	624	443	251
Hf	6.53	8.32	6.37	6.65	5.83	6.54	6.19	7.00	6.57	6.62	6.33	6.33	8.88	11.0	9.86	6.04
Y	38.5	31.8	30.8	31.3	28.7	29.5	26.2	34.3	31.1	34.5	33.1	27.7	31.0	40.5	36.8	31.0

sample	08KT 01	08KT 02	08KT 04	08KT 05	08KT 06	08KT 07	08KT 08	08KT 09	08KT 10	08KT 11	08KT 12	08KT 13	08KT 14	08KT 15
Rock type	B	B	B	B	B	B	B	B	**B**	B	B	B	B	B
Major elements (%)														
SiO_2	44.48	44.45	44.10	44.35	44.41	44.31	47.31	47.17	45.12	44.69	44.38	49.32	51.24	50.37
TiO_2	4.02	4.02	4.00	3.98	3.96	3.95	4.07	4.02	3.74	3.72	3.99	3.41	3.25	3.55
Al_2O_3	14.0	14.03	14.23	14.16	14.14	14.28	13.02	13.08	14.24	14.47	14.17	11.22	10.59	11.91
Fe_2O_3	17.0	17.01	17.04	16.96	16.90	16.94	16.23	16.24	15.53	15.56	17.05	17.14	17.44	18.15
MnO	0.20	0.20	0.20	0.20	0.19	0.19	0.20	0.21	0.18	0.18	0.19	0.18	0.16	0.13
CaO	5.73	5.73	5.85	5.84	5.69	5.90	4.45	4.68	6.19	5.64	5.81	3.67	3.35	3.72
MgO	7.83	7.98	7.93	7.92	8.12	7.82	7.99	8.05	8.43	8.45	7.91	6.12	5.26	4.00
K_2O	1.30	1.42	1.34	1.39	1.46	1.34	1.45	1.54	1.26	1.23	1.36	0.97	1.04	0.71
Na_2O	3.45	2.9	3.19	3.12	3.03	3.16	3.12	3.05	2.91	2.92	3.16	3.87	4.22	4.39
P_2O_5	0.97	1.01	0.95	0.95	0.96	0.94	0.99	0.95	0.73	0.71	0.95	0.62	0.56	0.62
LOI	0.43	0.75	0.67	0.70	0.71	0.74	0.79	0.61	1.22	1.99	0.62	3.15	2.60	2.17
Σ	99.5	99.58	99.58	99.58	99.58	99.58	99.61	99.62	99.56	99.55	99.58	99.67	99.72	99.71
$Mg^{\#}$	36	36	37	37	36	37	32	33	40	38	36	26	24	26
Trace elements (ppm)														
La	35.0	35.1	35.0	35.8		33.5	39.4	35.68	29.7	28.9	34.7	32.0	31.9	29.9
Ce	81.0	80.0	80.9	82.4		76.2	88.9	77.31	68.4	66.4	79.5	73.6	69.2	69.2
Pr	11.1	11.07	11.15	11.24		10.37	11.88	10.36	9.42	8.993	11	9.76	9.11	9.34
Nd	48.0	47.3	47.4	48.7		45.2	50.6	44.50	40.6	39.2	47.4	40.8	37.6	39.8
Sm	9.82	9.73	9.76	9.85		9.37	10.11	9.18	8.47	8.07	9.58	8.37	7.66	8.31
Eu	3.12	3.01	3.08	3.03		2.84	2.97	2.84	2.64	2.50	2.91	2.56	2.33	2.55
Gd	10.0	9.25	8.98	9.12		8.70	9.50	8.94	8.11	7.72	8.93	7.98	7.19	7.80
Tb	1.55	1.41	1.39	1.48		1.33	1.45	1.39	1.29	1.26	1.40	1.29	1.17	1.20
Dy	8.39	7.49	7.50	7.84		7.13	7.85	7.85	7.13	6.80	7.72	7.11	6.12	6.51
Ho	1.55	1.39	1.43	1.43		1.31	1.47	1.51	1.36	1.30	1.44	1.33	1.14	1.19
Er	4.12	3.64	3.80	3.86		3.47	3.95	3.92	3.61	3.44	3.95	3.47	3.03	3.26
Tm	0.62	0.54	0.56	0.57		0.50	0.59	0.54	0.54	0.52	0.58	0.50	0.47	0.49
Yb	3.63	3.31	3.57	3.50		3.18	3.64	3.48	3.38	3.18	3.61	3.08	2.87	3.05
Lu	0.60	0.56	0.60	0.55		0.51	0.57	0.53	0.54	0.52	0.58	0.51	0.47	0.49
Rb	23.6	23.4	23.0	24.4		22.2	15.8	23.6	23.8	23.4	24.3	17.8	16.5	12.9
Ga	22.7	20.6	21.6	23.0		20.7	22.3	21.7	22.8	22.9	22.4	16.3	12.8	19.8
V	209	217	221	228		222	222	237	220	208	235	212	181	208
Cr	60.9	63.3	61.1	66.4		66.2	27.8	66.58	78.4	77.7	64.9	10.3	13.9	10.2
Ni	70.4	65.6	74.6	84.3		71.6	32.9	68.54	74.2	79.0	72.2	16.9	18.8	16.9
Sc	23.5	24.5	24.4	25.3		25.3	24.0	24.0	24.1	24.8	19.7	19.1	19.9	23.5

Sr	352	328	420	352		334	310	484	298	303	355	191	164	183
Ba	621	670	689	724		658	768	687	554	548	706	831	707	492
Th	3.61	3.58	3.38	3.55		3.34	5.08	3.02	3.31	3.18	3.36	5.27	5.12	5.15
U	0.82	0.78	0.81	0.80		0.74	1.03	0.73	0.78	0.77	0.77	1.37	1.56	1.45
Ta	1.86	1.70	1.80	1.81		1.64	1.59	1.66	1.51	1.52	1.75	1.70	1.67	1.72
Nb	26.1	25.3	25.0	25.9		24.9	24.0	24.86	22.0	22.1	25.7	24.5	23.5	25.0
Zr	289	276	282	286		262	293	280	239	241	283	243	224	249
Hf	7.61	6.48	7.04	6.84		6.33	7.27	6.13	6.13	5.81	7.00	6.18	5.85	6.14
Y	39.9	37.9	38.8	38.5		36.3	39.4	38.12	35.6	36.2	38.7	36.9	30.4	32.3

sample	08KT02-1	08KT02-2	08KT02-3	08KT02-4	08KT02-5	08KT02-6	08KT02-7	08KT03-1	08KT03-2	08KT03-3	08KT03-4	08KT03-5	08KT03-6	08KT03-7	08KT03-8
Rock type	APG	APG	APG	APG	APG	APG	APG	APG	APG	APG	APG	APG	APG	APG	APG
Major elements (%)															
SiO_2	71.86	71.70	73.22	74.24	72.89	72.70	75.23	77.67	77.88	77.81	76.76	77.99	77.24	78.22	77.02
TiO_2	0.19	0.17	0.16	0.19	0.17	0.17	0.28	0.04	0.04	0.05	0.06	0.05	0.05	0.03	0.04
Al_2O_3	14.60	14.70	14.44	13.36	13.1	13.9	12.0	12.0	12.0	12.0	12.17	12.18	12.01	12.00	12.42
Fe_2O_3	1.91	1.74	1.47	1.76	1.62	1.75	2.73	0.42	0.26	0.40	1.15	0.49	0.77	0.21	0.70
MnO	0.03	0.03	0.03	0.03	0.03	0.03	0.05	0.01	0.01	0.01	0.01	0.01	0.02	0.01	0.01
CaO	1.20	1.14	1.00	0.96	0.89	1.01	1.15	0.53	0.59	0.52	0.57	0.47	0.52	0.49	0.53
MgO	0.15	0.14	0.15	0.15	0.15	0.15	0.18	0.05	0.05	0.08	0.07	0.08	0.05	0.07	0.07
K_2O	5.30	5.72	5.35	5.19	5.25	5.83	4.56	4.85	4.72	4.88	4.83	4.59	4.86	4.70	5.00
Na_2O	4.33	4.15	3.73	3.64	3.44	3.86	3.40	3.73	3.79	3.60	3.76	3.50	3.70	3.61	3.58
P_2O_5	0.02	0.02	0.02	0.03	0.02	0.02	0.04	0.01	0.00	0.00	0.00	0.00	0.00	0.01	0.00
LOI	0.15	0.21	0.21	0.24	2.20	0.29	0.20	0.42	0.38	0.43	0.43	0.46	0.58	0.48	0.45
Σ	99.74	99.73	99.76	99.79	99.8	99.7	99.8	99.8	99.8	99.8	99.81	99.84	99.80	99.82	99.81
Trace elements (ppm)															
La	48.11	86.2	96.2	108	42.6	52.4	78.4	56.0	64.7	61.7	65. 5	53.1	64.9	49.6	59.0
Ce	103.7	176	194	211	102	108	174	115	137	130	141	113	140	104	127
Pr	13.57	21.2	22.8	24.5	11.8	13.5	22.2	14.1	16.7	15.7	17.6	14.1	16. 9	13.3	15.5
Nd	54.6	77.1	80.8	85.7	45.4	52.5	85.4	48.9	58.5	54.9	64.3	50.4	60.6	48.2	55.3
Sm	11.3	13.3	13.0	14.3	9.17	11.8	16.7	10.3	12.5	11.7	15.4	11.2	13.2	10. 9	12.2
Eu	1.52	1.68	1.63	1.49	1.32	1.34	1.27	0.04	0.04	0.05	0.05	0.04	0.05	0.04	0.05
Gd	10.6	11.3	10.9	12.3	8.63	11.5	15.0	9.78	12.7	11.4	15.4	10.6	12.8	10. 8	12.5
Tb	1.81	1.78	1.64	1.94	1.52	2.11	2.59	1.89	2.42	2.19	3.09	2.04	2.48	2.09	2.41
Dy	10.14	9.76	8.64	10.4	8.72	12.1	14.4	11.5	14.2	12.8	18.8	12.0	14.5	12.3	14.4
Ho	1.88	1.84	1.59	1.99	1.68	2.27	2.78	2.31	2.86	2.49	3.81	2.41	2.94	2.44	2.82
Er	5.19	4.91	4.35	5.62	4.81	6.08	7.72	7.18	8.38	7.40	11.5	7.15	8.75	7.22	8.34
Tm	0.78	0.75	0.65	0.89	0.75	0.95	1.19	1.27	1.38	1.23	1.89	1.24	1.49	1.20	1.38
Yb	4.86	4.59	4.13	5.54	4.78	5.81	7.50	8.82	8.93	7.78	11.9	8.04	9.88	7.94	8.85
Lu	0.74	0.71	0.65	0.87	0.75	0.99	1.17	1.40	1.38	1.19	1.83	1.28	1.50	1.26	1.38
Rb	170	190	183	177	197	207	151	447	441	412	456	416	456	443	470
Ga	31.1	30.1	28	29.3	27.2	28.7	25.9	29.5	30.1	27.9	30.0	28.4	29.71	29.2	29.5
V	2.98	2.43	3.16	4.27	3.01	2.33	4.39	2.45	1.97	3.11	1.35	1.72	1.74	1.60	1.86
Cr	0.05	0.03	0.64	0.45	0.12	0.09	0.05	0.15	0.74	0.62	1.49	0.63	0.11	4.17	0.29
Ni	1.21	0.73	1.64	0.82	0.89	0.18	0.73	0.54	0.22	0.01	1.21	1.55	1.66	4.75	1.37

Sr	88.7	97.8	93.5	87.6	77.9	80.4	75.9	6.23	8.59	7.31	7.34	7.49	5.15	7.84	6.29
Ba	460	551	546	484	465	466	364	9.91	10.5	10.8	9.53	12.2	8.22	9.63	10.8
Th	17.6	20.6	20.3	26.6	17.1	12.8	27.4	41.1	41.7	40.1	53. 9	41.8	44.0	45.0	42.9
U	2.83	2.35	2.44	3.98	3.46	5.64	3.80	5.90	9.32	7.32	7.62	9.94	7.79	9.34	5.97
Ta	3.04	3.17	2.93	4.07	3.81	4.51	4.71	6.99	9.17	7.81	8.34	9.74	8.76	8.85	7.67
Nb	44.7	44.2	40.7	52.6	50.2	59.1	69.3	82.4	115	97.5	143	116	105	108	92.1
Zr	367	183	243	314	266	172	367	234	164	176	202	206	210	178	172
Hf	10.6	5.61	7.22	9.81	8.10	5.50	11.9	13.1	9.51	9.00	11.1	11.3	12.0	10.3	9.16
Y	52.8	50.5	45.2	56.4	48.6	61.9	76.7	77.9	91.2	77.4	121	73.9	91.5	78.4	90.7

MGB-magnetite –(bearing) gabbro; MQGB- magnetite and quartz – bearing gabbro; PGB – plagioclase-rich gabbro; QGB – quartz – bearing gabbro; OMGB – olivine and magnetite –bearing gabbro; DB – diabase or dolerite; B- basalt; APG – alkali-feldspar granite

2.1	188	80	0.44	0.48	.0439	2.1	0.36	4.5	0.0600	4.0	274.1	5.6	604	87
3.1	115	78	0.70	0.99	.0453	2.2	0.40	9.9	0.0648	9.6	281.0	6.3	767	203
4.1	270	91	0.35	0.29	.0449	2.0	0.37	4.1	0.0599	3.6	280.7	5.6	601	77
5.1	506	233	0.48	0.42	.0438	2.0	0.45	4.3	0.0738	3.9	269.0	5.3	1037	78
6.1	239	104	0.45	0.26	.0443	2.0	0.39	4.1	0.0645	3.5	275.3	5.5	758	74
7.1	80	30	0.39	1.11	.0431	2.4	0.48	10.3	0.0808	10.0	262.7	6.1	1216	197
8.1	197	88	0.46	0.65	.0452	2.0	0.44	7.3	0.0704	7.0	278.5	5.8	939	143
9.1	132	53	0.42	0.51	.0457	2.1	0.47	7.4	0.0745	7.1	280.5	6.0	1055	144
10.1	213	99	0.48	0.12	.0427	2.0	0.41	5.1	0.0688	4.7	263.8	5.4	894	98
11.1	240	94	0.41	0.14	.0432	2.0	0.41	2.9	0.0694	2.1	266.9	5.3	912	43
12.1	235	116	0.51	0.17	.0424	2.0	0.35	3.0	0.0594	2.2	265.2	5.3	580	49
13.1	115	46	0.41	0.64	.0432	2.1	0.45	9.2	0.0753	8.9	265.1	6.0	1076	179
14.1	260	112	0.45	0.10	.0448	2.0	0.41	6.6	0.0665	6.3	277.6	5.7	823	131
15.1	211	95	0.46	0.17	.0433	2.0	0.43	7.3	0.0713	7.1	266.8	5.6	965	144
16.1	160	86	0.55	0.00	.0457	2.1	0.49	7.7	0.0772	7.4	279.2	6.1	1126	147
17.1	340	140	0.43	0.00	.0437	2.0	0.39	6.8	0.0644	6.5	271.7	5.5	756	136

f_{206}: percentage of common ^{206}Pb in total ^{206}Pb

Table.3 Nd isotope compositions of the coeval diverse igneous rocks along the north margin of Tarim

Sample	Sm (ppm)	Nd (ppm)	$(^{147}Sm/^{144}Nd)_c$	$(^{143}Nd/^{144}Nd)_m$	$2\sigma_m$	εNd(t) (t=275Ma)
Permian basalts						
08KT01	9.82	48	0.1237	0.512384	0.000008	-2.39
08KT04	9.76	47.4	0.1245	0.512391	0.000007	-2.28
08KT07	9.37	45.2	0.1253	0.512378	0.000007	-2.57
08KT10	8.47	40.6	0.1261	0.512395	0.000007	-2.26
08KT11	8.07	39.2	0.1245	0.512392	0.000007	-2.26
08KT12	9.58	47.4	0.1222	0.512392	0.000007	-2.18
08KT13	8.37	40.8	0.1240	0.512402	0.000007	-2.05
08KT14	7.66	37.6	0.1232	0.512395	0.000008	-2.16
Piqiang ultramafic-mafic complex						
08KT01-1	1.06	4.187	0.1531	0.512666	0.000008	2.08
08KT01-2	0.579	3.06	0.1144	0.512436	0.000008	-1.05
08KT01-5	1.663	6.471	0.1554	0.512588	0.000007	0.48
08KT01-8	1.34	4.22	0.1920	0.512592	0.000010	-0.73
08KT01-9	2.67	10.01	0.1613	0.512536	0.000008	-0.75
08KT01-15	7.884	38.88	0.1226	0.512484	0.000008	-0.40
08KT01-11	5.184	21.82	0.1436	0.512571	0.000006	0.56
Bachu mafic dykes						
08KT16-1	11.44	60.48	0.1144	0.512747	0.000008	5.02
08KT17-1	8.464	40.56	0.1262	0.512674	0.000008	3.18
08KT18-1	9.02	46.4	0.1175	0.512524	0.000008	0.56
08KT18-9	8.61	42.1	0.1236	0.512762	0.000007	4.99

Sample	Sm (ppm)	Nd (ppm)	$^{147}Sm/^{144}Nd$	$^{143}Nd/^{144}Nd_m$	$2\sigma_m$	T_{DM} Ga	T_{2DM} Ga	εNd(t) (t=275Ma)
08KT02-4	15.4	64.3	0.1448	0.512438	0.000008	1.6	1.2	-2.08
08KT02-5	11.1	50.4	0.1331	0.512431	0.000006	1.4	1.2	-1.81
08KT02-7	10.8	48.1	0.1357	0.512422	0.000007	1.4	1.2	-2.07
08KT03-1	11.2	54.6	0.1240	0.512496	0.000007	1.1	1.1	-0.22
08KT03-3	13.01	80.85	0.0973	0.512439	0.000007	0.9	1.1	-0.39
08KT03-7	16.6	85.4	0.1175	0.512479	0.000007	1.1	1.1	-0.32

$2\sigma_m$ = 2-sigma-mean error.

Table. 4 Age data of the Permian igneous rocks along the northern margin of Tarim

Location	Rock	Mineral	Method	age（Ma）	Reference
Mazhaertage	Syenite	Whole rock	$^{39}Ar/^{40}Ar$	278 ± 1	Yang et al., 1996
Mazhaertage	Syenite	Zircon	SHRIMP	277 ± 4	Yang et al., 2006
Keping	Basalt	Whole rock	$^{39}Ar/^{40}Ar$	279 ± 1	Chen et al., 1997
Central Tarim	Tuff	Whole rock	$^{39}Ar/^{40}Ar$	276-288	XOAC, 2003
Keping	Basalt	Zircon	LA-ICP-MS	275 ± 13	Li et al., 2007
Keping	Tuff	Zircon	LA-ICP-MS	291 ± 10	Li et al., 2007
Kepjng	Gabbro	Zircon	LA-ICP-MS	274 ± 15	Li et al., 2007
Mazhaertage	Diabase	Zircon	LA-ICP-MS	272 ± 6	Li et al., 2007
Mazaertage	Diabase	Zircon	LA-ICP-MS	282 ± 3	Li et al., 2007
Mazaertage	Syenite	Zircon	LA-ICP-MS	281 ± 4	Li et al., 2007
Mazhaertage	Gabbro	Zircon	LA-ICP-MS	274 ± 2	Zhang et al., 2008
South of Akesu	Rhyolite	Zircon	LA-ICP-MS	277.3±2.5	Tian et al., 2010
South of Akesu	Rhyolite	Zircon	LA-ICP-MS	290.9±4.1	Tian et al., 2010
South of Akesu	Rhyolite	Zircon	LA-ICP-MS	286.6±3.3	Tian et al., 2010
South of Akesu	Rhyolite	Zircon	LA-ICP-MS	282.9±2.5	Tian et al., 2010
South of Akesu	Rhyolite	Zircon	SHRIMP	271.7±2.2	Tian et al., 2010
Piqiang complex	Ganbbro	Zircon	SHRIMP	276 ± 4	This study
Halajun pluton □	Granite	Zircon	SHRIMP	278 ± 3	This study
Halajun pluton □	Granite	Zircon	SHRIMP	278 ± 3	This study